Infraslow fluctuations and respiration are driving cortical neurophysiological oscillations during sleep

Tommi Väyrynen

Master's thesis

Faculty of Science, Study Program of Physics

Oulu Functional Neuroimaging

NANOMO, Biomedical physics

University of Oulu

2022

Abstract

Recently sleep has been linked to increased brain clearance through perivascular spaces from blood-brain barrier (BBB) externa limitans, facilitated by physiological pulsations such as cardiovascular and respiratory pulsations. Infraslow fluctuations (ISFs) characterize both fMRI BOLD signals and scalp EEG potentials. They are associated with both permeability fluctuations of BBB and the amplitude dynamics of faster (> 1Hz) neuronal oscillations. ISF together with respiration are though to synchronize with neural rhythms, however the directionality of these interactions has not been studied before. I used non-invasive measures which are necessary not to interfere the pressure sensitive CSF convection and BBB permeability combined with directional metrics to fully evaluate these relationships. I recorded full-band resting state EEG (fbEEG) during wakefulness and sleep and investigated whether recently shown increased brain clearance during sleep is followed by increased drive of neural amplitudes by the ISF and respiration phases. I show that ISF power increases during non-REM sleep, possibly reflecting altered BBB status. Furthermore, I show that ISF and respiration phase-amplitude couple and predict neuronal brain rhythms seen especially during sleep. These results pave the way for understanding the mechanisms how neuronal activity is modulated by the slow oscillations in human brain during wakefulness and sleep.

List of abbreviations

AAC	Amplitude-amplitude correlation
BBB	Blood-brain barrier
BOLD	Blood oxygen level dependent
CFS	Cross-frequency phase synchrony
CNS	Central nervous system
CSF	Cerebrospinal fluid
DC	Direct current
ECG	Electrocardiogram
EEG	Electroencephalogram
FDR	False discovery rate
FFT	Fast Fourier transform
fMRI	Functional magnetic resonance imaging
IC	Independent component
ICA	Independent component analysis
IF	Interstitial fluid
ISF	Infraslow fluctuation
MEG	Magnetoencephalography
NREM	Non rapid eye movement
PAC	Phase-amplitude coupling
PCA	Principal component analysis
PLV	Phase locking value
PTE	Phase transfer entropy
REM	Rapid eye movement
TE	Transfer entropy

Table of contents

Introduction

Early sign of drowsiness in healthy adults is characterized by mild slowing of EEG alpha rhythm and increase in its power. As the drowsiness deepens, low voltage activity composed from 2-7 Hz frequencies interrupt alpha activity, until completely replacing it, usually referred as alpha dropout [1]. In light sleep, sleep spindles and K-complexes appear. Transition to deeper sleep introduces slow waves that take the place of dominant rhythm [2]. However, the most salient EEG power occur at the very lowest frequencies in full-band EEG known as infraslow fluctuations (ISF < 0.1 Hz) [3]. During NREM sleep, infraslow fluctuations have been shown to increase [4], [5].

It has been under debate where do these very slow oscillations arise. Conventional theories have proposed glial cells such as astrocytes. More recent experiments showed that spatial extent and magnitude of these oscillations likely rule out glia networks and proposed a new model to explain observations. This model stated blood-brain barrier (BBB) as a source of ISF observed with EEG [6]. BBB is a barrier mechanism found inside central nervous system capillaries, which maintains brain homeostasis and acts as physical barrier for toxins. Tight junctions found at BBB have very high electrical resistance which makes it possible to maintain large transcellular potentials. These tight junctions and especially opening of the junctions can generate millivolt scale potentials detectable on the scalp with EEG recordings [6], [7].

Sleep is known to have several immunologic and metabolic functions and has been recently linked to increased brain tissue washout through perivascular spaces from BBB externa limitans [8]. This model known as the glymphatic model, serves similar function as lymphatic system outside central nervous system, disposing potentially harmful water-soluble substances contained in CSF [9]. In the process CSF and interstitial fluid are interchanged as convective flux drives fluid from para-arterial toward para-venous spaces, where it ultimately reaches lymph nodes of the neck and is returned to systemic circulation. This is the main pathway for clearance [10] along with substantial clearance through the BBB [11], [12]. Physiological pulsations such as cardiac and respiratory pulsations have been shown to mediate the clearance in para-arterial spaces in the direction of blood flow [13].

It is known that BBB permeability changes are reflected into EEG ISF power [6], [7], [14] and that ISF is phase-amplitude coupled to cortical amplitudes over wide range of frequencies [15], seen during NREM sleep. However, the directionality of this phase interaction is still unknown. Respiration is also known to synchronize with neural amplitudes [16] but as with ISF, the directionality and how sleep alters the scheme is still unclear. Invasive probing interferes with the sensitive CSF convection and BBB permeability [17]. Therefore, the assessment of both BBB permeability and interstitial status needs to be derived from non-invasive measures. To properly assess the

relationship between ISF phase and cortical amplitudes, a metric that takes directionality into an account is needed.

I used 256-channel EEG system to non-invasively quantify sleep induced changes in both power and phase interactions between physiological and neuronal activity. I localized the power and coupling changes using phase-amplitude coupling (PAC) and phase locking value (PLV) as a metric for the synchronization. Finally, to determine the directionality of the interaction I used phase transfer entropy (PTE); an information theory-based phase-specific measure of effective connectivity. I hypothesized that if the BBB permeability increases in sleep, the cortical neuronal amplitudes would become increasingly driven by the ISF phase.

I show that spectral power of physiological pulsatility is increased during sleep, especially slow-wave and infraslow frequency EEG (ISF_{EEG}) power, implying increased permeability and clearance over the BBB. I demonstrate that ISF and respiration are both phase-amplitude coupled to cortical EEG rhythms. My analysis further revealed that ISF and respiration are not only coupled but also predicting the neuronal rhythms.

Background

Sleep

Most adults require 7-8 hours of sleep on average, equalling about third of a day. This number varies throughout life, in a way that older people tend to sleep more lightly and shorter times. Since sleep as a behaviour has persisted in every animal species suggests that it serves purposes crucial for normal function, all of which are not known yet. It seems that there are multiple purposes for sleep including: metabolic, immunologic, and memory related reasons. For example, brain glycogen levels which are exhausted during the day are replenished during sleep. In humans, lack of sleep leads to impaired memory, declined cognitive abilities, mood swings and hallucinations. In severe cases of fatal insomnia, the patients die within several years of onset due inability to enter deeper sleep stages. [18]

Cortical activation necessary to maintain wakefulness is supported by ascending arousal system. This system comprises of subcortical structures and pathways which release neurotransmitters such as norepinephrine, serotonin, histamine, dopamine, acetylcholine, and orexin. All of these seem to be important, supporting the function of the ascending arousal system. For example, lack of orexin secreting cells is known to be responsible for narcolepsy, resulting in sleep fragmentation, cataplexy, and excessive sleepiness during daytime. Sleep-wake cycle is controlled by circadian pacemaker, the suprachiasmatic nucleus with the help of external cues i.e., the amount of light [19].

Activation of suprachiasmatic nucleus evokes response in pineal gland which synthesizes melatonin (sleep-promoting neurohormone) from tryptophan [18]. Melatonin is secreted into the bloodstream where it modulates the brainstem circuits governing the sleep-wake cycle [18]. In addition to circadian drive also homeostatic effects drive and maintain sleep [19]. Sleep is not only a state of diminished brain activity, but rather a series of tightly controlled brain states. Suppression of ascending arousal system is needed to initiate sleep. This is done by inhibitory neurons located at ventrolateral preoptic area, which remain active throughout night to maintain sleep [2].

Sleep hierarchy can be split into two main components: NREM-sleep and REM-sleep that is associated with dreaming. NREM-sleep branches even further according to depth of the sleep, which can be quantified with EEG. REM and NREM sleep experience cycling pattern usually within intervals from 60 to 90 minutes. This is thought to be controlled by activation and inhibition of 'REM-on' cholinergic neurons found inside brainstem. [2]

During sleep onset several physiological and behavioural changes take place. Most obvious change is loss of consciousness and reduced tonus of skeletal muscles. But also reduced breathing, heart rate, temperature, blood pressure and metabolism [18]. Many sensory responses are minimized during NREM sleep but can experience different features during REM sleep. Multiple physiological features such as blood pressure and heart rate suddenly increase during REM sleep [18]. Skeletal muscle activity follows decreasing amplitude as sleep depth increases [2].

Changes that take place during sleep can be monitored using many different measures. One can measure the physiological changes in heart rate for example. Sleep laboratories utilize multiple measures to fully assess sleep and sleep disorders. Most comprehensive tool for sleep research so far has been the EEG. With the help of EEG, Kleitman and Aserinsky (1953) showed that sleep is not uniform but experiences different stages during night [20]. What they discovered was REM sleep.

Field potentials and rhythms

The EEG signal is generated by specialized neurons called pyramidal neurons located at cerebral cortex. This was experimentally shown by animal studies, which noted a reversal in the electrical field when passing an electrode vertically from the surface of the cortex to white matter [18]. It is not action potentials of neurons which generate the signal but rather the graded post-synaptic potentials. Pyramidal neurons are main contributors of signal since they are arranged perpendicular to surface of the cortex and parallel to each other. When simultaneously activated, this arrangement allows large enough extracellular current flow to be generated and measured at the scalp. Measured potential is summation of longitudinal components from large population of neurons. The transverse components cancel each other out on a macroscopic scale [21]. Since

axons carrying the action potentials are not typically oriented parallel and perpendicular to surface in addition to short lasting of action potentials and relatively unsynchronized firing, strong enough signal cannot be generated even if cancelling out does not take place [21].

The extracellular potentials, commonly known as field potentials, are generated by postsynaptic potentials, which take place in the synaptic cleft after neurotransmitter release. If action potential travels along a fibre ending in excitatory synapse, an excitatory postsynaptic potential (EPSP) occurs in postsynaptic neuron. If the action potential travels to inhibitory synapse, then inhibitory postsynaptic potential (IPSP) takes place, resulting in hyperpolarization [3]. These two postsynaptic potentials: excitatory (EPSP) and inhibitory (IPSP) will lead to either outward or inward current flow across the membrane, depolarizing or hyperpolarizing membrane potential making the cell more or less likely to generate action potential [3], [21].

This synaptic current flow is accompanied by an opposite transmembrane flow inward or outward at another location in the dendritic tree, which then generates a dipole. The orientation of this dipole depends on the type of synaptic activity (EPSP or IPSP), and also the location of the synapse, whether it is superficial or deep. EPSP and IPSP create opposite dipoles when the location of the synapse is on the same level. Superficial EPSP produces a dipole with negative pole closer to surface and positive pole deeper. Deep EPSP creates and opposing dipole compared to superficial EPSP, with positive superficial pole (Figure 1). Synchronous activation of many pyramidal neurons then behaves like dipole layer on a macroscopic level. [21]

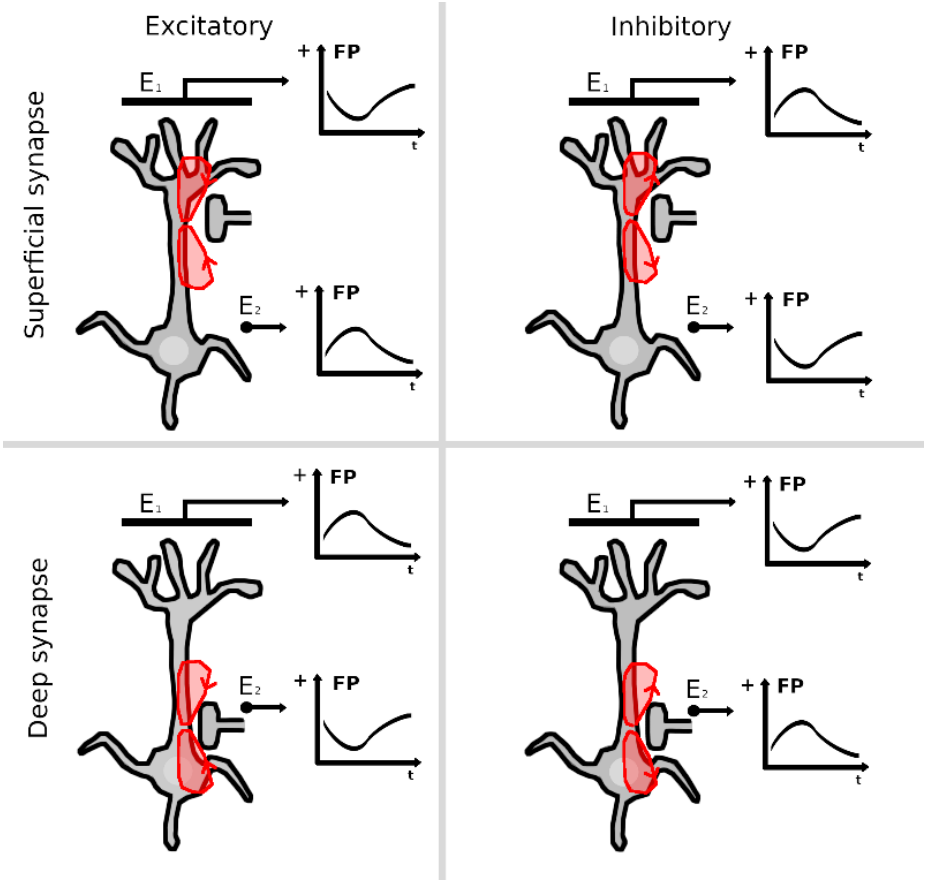

Figure 1. Generation and direction of field potentials are dependent on type and location of synapse. Field potentials measured by electrodes E_1 and E_2 are shown in the graphs. Red lines indicate the direction of current flow. Recreated from: Niedermeyer's electroencephalography: basic principles, clinical applications, and related fields. Neurophysiologic Basis of EEG and DC Potentials, p.4, Figure 2.5.

In addition to neurons, non-neural cells such as glial cells can generate field potentials. Since glial cells are non-neural cells, they don't have synapses and hence cannot generate action potentials. However, the membrane potential of glial cells is highly regulated by potassium concentration. Neuronal activation is accompanied by outflow of potassium, due to this glial cell membrane potential essentially follows neural activation. Glial cells are usually connected to each other over wide areas, enabling them to generate field potentials with considerable spatial extent. [3]

Reciprocal interaction of excitatory and inhibitory neurons in circuit loops generate oscillations with unique frequency ranges at different brain regions [18]. These rhythms can be characterized by their unique frequency range and location of appearance. But also, by their shape and onset circumstances. Common frequency ranges studied and used clinically are delta (1-4 Hz), theta (4-8 Hz), alpha (8-13 Hz), beta (13-30 Hz), and gamma (>30 Hz) frequencies. They can reveal information about brain state and function during different tasks or arousal states. The onset of sleep drastically changes the

composition of EEG. Before actual NREM sleep there is a period of drowsiness, which is the first step into the sleep. During this period slow rolling eye movements can be seen which are also reflected into frontal electrodes in EEG. The first (N1) stage is characterized by dampening of alpha (8-13 Hz) rhythm and emergence of theta (4-8 Hz) rhythm. Second stage (N2) is seen as emergence of sleep spindles (11-16 Hz) and at frontal cortex unique shaped biphasic waves called K-complexes. Deep sleep (N3) can be easily identified with presence of slow delta (1-4 Hz) waves. Surprisingly the REM sleep can exhibit similar EEG patterns as during wakefulness in addition to sawtooth waves of delta frequency. [2]

Glymphatic system

Metabolic by-products in the body are removed by the lymphatic vessels, running in parallel with the blood vascular system. These vessel act as a pathway, into which excess fluid and proteins are disposed. As arteries deliver blood down to smallest capillaries, blood plasma and proteins are forced into the interstitial space, where most get reabsorbed by capillary venules [22]. What is left is absorbed to lymphatics capillaries, from where it is eventually returned back into circulatory system. Without lymph vessels excess plasma would start to accumulate into the interstitial spaces. While maintaining the proper fluid balance in tissues, lymphatics also serve as transport route for immune cells and interstitial proteins [22]. Lymphatic system spans throughout the whole body except for spinal cord and brains. The lack of lymphatic vessels in the brain is interesting, since neurons have high metabolic rate, which leads to high demand for disposal of these metabolic by-products.

Cerebrospinal fluid (CSF), found deep inside brain at ventricles and also between the skull and brain in subarachnoid spaces, was though for long to serve a purpose of sink into which waste products can diffuse. However, long diffusion times from most parts of brain makes this process inefficient e.g., albumin would require over 100 hours to diffuse 1cm distance in brain tissue [9]. Later two-photon imaging revealed that CSF is exchanged rapidly with IF i.e., the fluid in the extracellular spaces of the cells. CSF enters trough para-arterial space surrounding the arteries. Aquaporin-4 (AQP4) water channels located at astrocytic endfeet facilitate this convective flow out of para-arterial spaces and into the interstitial space. As CSF and IF are interchanged, convective flux drives the waste products from the arteries toward veins (Figure 2). The IF containing waste products then enter para-venous spaces, from where it exits the brain along para-venous route. Eventually it reaches the lymphatic nodes of the neck, from where it returns its contents into the systemic circulation, where it ultimately reaches the liver [9]. This model of CSF and IF interchange is called glymphatic system, where its name refers to lymphatic system due to their similar purpose and aquaporin channels which are essential to CSF and IF exchange. [23]

BBB refers to unique properties of the capillaries in brain endothelium. These properties allow vessels to tightly regulate movement of ions, molecules and even cells between the blood and the brain. This strict regulation and control of CNS homeostasis is crucial for proper neural function and protects brain from harmful toxins and pathogens. The walls of the blood vessels are made of endothelial cells. Astrocytic endfeet, where aquaporin channels are located, cover the entire capillary surface forming additional barrier on the capillaries. Unlike capillaries in the peripheral system, in CNS the endothelial cells are connected by tight junctions. Majority of BBB properties arise from these tight junctions. Cells surrounding the capillaries such as astrocytes or even neurons can also control and modulate the function of BBB. Therefore, BBB can be though as neurovascular unit. Before discovering of glymphatic system it was thought that the main route for brain clearance is through BBB. [24]

Glymphatic system and BBB serve the same purpose in clearing interstitial metabolites, with overlapping mechanisms and therefore act as complementary roles. When the distances to BBB are too large for efficient clearance, the by-products must be cleared through IF flow in glymphatic system. During wakefulness the interstitial space is dense with relatively high resistance to convective flow (bulk flow) and CSF movement. However, during sleep the volume of interstitial space increases, facilitating CSF and IF exchange and making the glymphatic clearance more efficient. Increased convective flow also indirectly increases the BBB clearance by pushing the waste molecules towards BBB. Disruption of one these mechanism leads to protein accumulation in the brain and could be responsible for neurodegenerative diseases, such as Alzheimer's disease. [25]

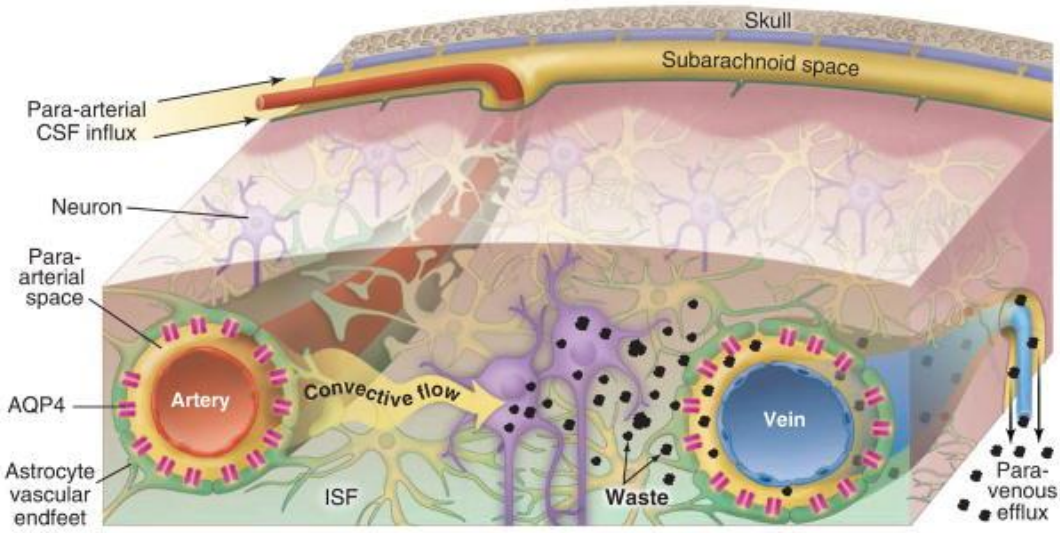

Figure 2. Glymphatic system of the human brain. Neuronal metabolic waste is pushed by convective glymphatic flux from para-arterial into the para-venous space, where it is directed into general circulation. From "Neuroscience. Garbage truck of the brain." by Nedergaard,

Maiken, 2013, *Science, vol.* 340*,* p. 1529. Copyright: American Association for the Advancement of Science. Republished with permission.

Infraslow EEG fluctuations

Infraslow EEG fluctuations (ISF) are brain oscillatory rhythm with maximal spectral power in the frequencies below 0.1 Hz and irregular expression. Due its very low frequency expression, the time scales of one cycle can go up to several minutes. They are also known as DC-potentials, due to their recording setup involving DC -coupled amplifier, giving impression of constant baseline, which they aren't. They were first discovered with rabbits using intracranial electrodes in 1957 [26]. Formerly ISFs were thought to arise from cortical neurons and glial cells [27], [28]. However, recent studies have proposed also non-neuronal mechanism mainly the blood-brain barrier.

Conventionally EEG amplifiers have been equipped with inbuilt high-pass filters, to overcome the issue of slow electrode drifts that led to saturation of the amplifiers dynamic range. Since the development of direct current coupled amplifiers, it has been possible to record these infraslow frequencies. Recording of a full-band EEG (also known as DC-EEG) differs from conventional EEG recordings. Technical limitations are set to detect infraslow events, both to amplifier and electrode-skin interface. Electrode material needs to be nonpolarizable such as Ag/AgCl for stable DC -potential. Skin borne signals caused by galvanic reactions and electrode movements can be suppressed by short-circuiting the skin. This is achieved by scraping the surface of the skin under the electrode. Amplifier is required to be DC-coupled, meaning that recording is carried out using infinite time constant. Also, high input impedance, dynamic range preferably in range ±100mV are needed. Different time constants used in DC-EEG amplifiers compared to conventional EEG measurements, might also lead to distortion of faster potential components in the time domain. [3], [29]

ISFs are especially seen during NREM sleep [4], [5]. They are known to modulate the amplitude of cortical rhythms most notably delta (1-4 Hz) and sigma (10-20 Hz) bands [15], [30] which are also major components of non-REM sleep. Modulations have been also reported in theta [15], [31], alpha [31], and gamma [32] frequency bands. Since ISF phase modulates neural amplitudes over wide range of frequencies they reflect fluctuations of gross cortical excitability [15].

Until recent years it was thought that ISFs are mainly generated by cortical neurons and glial cells [27], [28], and they were measured in various events including epileptic discharges [28], [33] and spreading depression [34]. However, during epileptic discharges and spreading depression the brain pH changes. It has been confirmed many times that between CSF and blood there is a large pH sensitive trans-endothelial potential with humans and animals [35]–[37]. Therefore, during epileptic discharges and

spreading depression changes in brain pH makes it difficult to evaluate the weight of neurons/glia versus pH to the recorded ISF potentials. Using different ventilation manoeuvres such as hyperventilation, brain pH can be altered. During these tasks large ISF within brain tissue and in extracranial EEG were seen, confirming that change in brain pH elicits ISF_{EEG} potentials [38].

Hyperventilation decreases partial pressure of CO_2 and causes pH changes in extracellular fluid. This leads to arterial vasoconstriction and therefore lowers cerebral blood flow. ISFs have been shown to correlate with changes in cerebral blood flow [6], [39]. Animal studies with invasive measures [28] have shown that ISF are often absent with intracortical current loops responsible for higher rhythmical EEG activity, possibly indicating different generation mechanism. Hyperventilation induced ISF_{EEG} changes are in the millivolt range, which is several orders larger than conventional brain rhythms and far too large to be achieved by purely neuronal generators [6]. In humans disrupting the BBB with hyperosmolar intra-arterial mannitol infusion induces 2 mV ISF potential shift. These human treatments were made in deep anaesthesia with absent neuronal activity [7], implying that neuronal activation is not needed in ISF generation. In addition, large spatial spread and the duration of ISFs favour the involvement of subcortical structures [6]. It is therefore likely that ISF potential involves non-neuronal generator, mainly permeability changes of BBB.

Blind source separation

EEG recordings are always capturing signal from multiple sources simultaneously and due to way, which electrical fields transmit through various tissue layers such as such as skull and scalp causes multiple electrodes to record signal from the same source with different weights. The signal is always weighted sum of activity over larger and even multiple areas. It is possible to separate this mixed signal using computational methods to observe the underlying original phenomena. Commonly used methods are principal component analysis (PCA) and independent component analysis (ICA) and they are commonly used in various fields including finance, medical imaging, and seismology (Figure 3). Classical example is the 'cocktail party problem' which gives concise way of understanding the problem: There is a group of people talking in the room simultaneously. Several microphones are placed at various locations, all picking up mixed signals with different weights. Blind source separation techniques can be applied for mixed signals to extract individual speech tracks. With EEG there are several advantages of using blind source separation techniques. Common practice is to study the independent components with limitation that precise spatial location is lost in the process. Second way is used to improve signal quality where artificial components are identified and then removed from the mixed signal. [40]

ICA is a probabilistic method for determining linear transformation of a random vector. ICA searches components for which the independence and non-normality is maximized. Since it is data-driven method, there is no need to categorize the data in any way. Let $x_i(t), i = 1, \dots, n$ be the observed variables over the time interval $t = 1, \dots, T$. The signal $x_i(t)$ represents the measured signal, that is the mixed signal, in my case the EEG. Next an assumption is made, stating that signal can be modelled as a linear combination of unknown coefficients a_{ij} and hidden variables $s_j(t), j = 1, \dots, m$. Resulting in:

$$x_i(t) = \sum_{j=1}^{m} a_{ij} s_j(t) \text{ , for all i} = 1, \dots, \text{n.}$$

The $s_i(t)$ are the independent components and a_{ij} are so called mixing coefficients which are both to be estimated. Equation above is more convenient to represent in matrix form. Let $\boldsymbol{x}$ denote the observations $x_i(t)$ and $\boldsymbol{s}$ independent components $s_j(t)$, so that $\boldsymbol{x}$ and $\boldsymbol{s}$ are column vectors. Unknown mixing coefficients a_{ij} are represented in matrix $\boldsymbol{A}$. Using these notations, we can write the mixing model in form: $\boldsymbol{x} = \boldsymbol{A}\boldsymbol{s}$. If one were to know the mixing parameters $\boldsymbol{A}$, the linear equation would be easily solved just by inverting the linear system. However, since both $\boldsymbol{A}$ and $\boldsymbol{s}$ are unknown the problem becomes undetermined and more difficult to solve. What distinguishes ICA from PCA and factor analysis is that the non-gaussian structure of the data is considered. This so called higher-order statistical information can be utilized and used for separation of the independent components (IC), which cannot be done with PCA or factor analysis.[40]

Three basic restrictions are needed so that the ICA model can be estimated:

1. The independent components are assumed to be statistically independent
   The independence of the random variables y_i can be tested using probability densities, which are independent if joint probability density function $p(y_1, y_2, \dots, y_n)$ can be expressed as the product of the marginal probability density functions $p(y_1, y_2, \dots, y_n) = p(y_1)p(y_2) \dots p(y_n)$
2. The independent components must have non-gaussian (non-normal) distributions. ICA is essentially impossible if the components contain no higher order cumulants. The distributions are too simple to extract components.
3. Last assumption is that the mixing matrix $\boldsymbol{A}$ is square matrix, meaning that number of ICs are equal to the number of observed mixed signals. However, this criterion can be relaxed and therefore is not necessary, but it simplifies the problem. From this restriction follows that for the mixing matrix $\boldsymbol{A}$ exist also an inverse matrix $\boldsymbol{A}^{-1}$.

In the case that all the three assumptions hold the independent components can be easily solved after estimation of the mixing parameters:

$$\boldsymbol{s} = \boldsymbol{A}^{-1}\boldsymbol{x}$$

There are a few indeterminacies that result from equation above and need to be considered. Firstly, one cannot determine the variance (energy) of the ICs. This results directly from the reason that both $\boldsymbol{s}$ and $\boldsymbol{A}$ are unknown and therefore any scalar

multiplier in one of the sources $\boldsymbol{s}$ could be cancelled by division by the same scalar in the corresponding column of $\boldsymbol{A}$. Furthermore, what follows is also ambiguity of the sign: one could add -1 multiplier to the IC without affecting the model. Secondly, the order of the ICs cannot be determined due to same underdetermined reasons. One can freely change the ordering of the terms and call any of the components the first one. [40]

ICA algorithms estimate the separating matrix $\boldsymbol{W} = \boldsymbol{A}^{-1}$ that gives the independent components. It cannot be solved in a closed form, whose values could be directly evaluated. Instead, the solution is based on cost functions or objective functions. Solutions are found at the minima and maxima of these functions. Sophisticated iterative optimization algorithms are needed in the process. Some well-known ICA algorithms include infomax, FastICA, JADE and SOBI. All of the previous methods can be divided into two families by their methodology: maximization of non-gaussianity and maximum likelihood estimation. The non-Gaussian branch is governed by the central limit theorem, which states in the context that sums of non-Gaussian random variables are typically closer to gaussian than the original ones. Non-gaussianity is at its maximum when the linear combination of observed variables equals one of the independent components, which can be tested by calculating kurtosis or alternatively with approximation of negentropy. Maximum likelihood estimation or the information-theoretic alternative of minimizing the mutual information, relies on measuring variables such as maximum entropy. [40]

Before separating-matrix $\boldsymbol{W}$ can be estimated, a few preprocessing steps are needed. The two compulsory steps are centering and whitening. It is often preferable to perform low-pass filtering to reduce amount of noise or high-pass filtering to increase independence and non-gaussianity of the components. Also, combination of the two can be used i.e., band-pass filtering. On high dimension data, where number of true ICs might be smaller than the number of mixed signals, a necessary step might include dimension reduction of the data by PCA. This prevents overlearning of the model and further decreases the amount of noise. [40]

Estimation of ICs becomes easier with assumption that mixed variables and ICs have zero mean. Centering is done if the assumption of zero mean doesn't hold. This is done by subtracting sample mean from the observable variables. Due to this, ICs have zero mean as well. The mixing matrix is not affected by the operation. After the estimation of the mixing matrix and the ICs, the subtracted mean can be reconstructed back. [40]

A zero-mean random vector $Z = (z_1, .., z_n)^T$ is considered *white* or *sphered* if its elements z_i are uncorrelated and have unit variances. Good example of this is white noise, where there are no temporal correlations involved. The process of whitening is basically decorrelation which is then followed by scaling. It suppresses the first and second order information, allowing ICA to focus on the higher order statistics. Whitening can be done using principal components analysis. [40]

PCA can be used not only for whitening but also for reducing the data dimension. With PCA the estimated components are required to be uncorrelated, in comparison to ICA where the requirement is independence, independence being more strict criteria of the two. The redundancy introduced by correlations is removed by finding a rotated orthogonal coordinate system so that the measurements $\boldsymbol{x}$ are uncorrelated in the new coordinate system. Simultaneously variances of $\boldsymbol{x}$ are maximized on the new coordinate system.[40]

Couple of benefits arise from reducing the dimension. It decreases the amount of noise, especially in the case where number of signal sources is smaller than the number of mixtures. Another factor is that it prevents overlearning, meaning that there are too many parameters in the model with respect to number of available data points. Question that arises then is how many components need to be estimated. There is no simple answer to this question. One way is to pick the number of components which explain the data variance well enough for example 90 %. Typical approach is still by trial and error.[40]

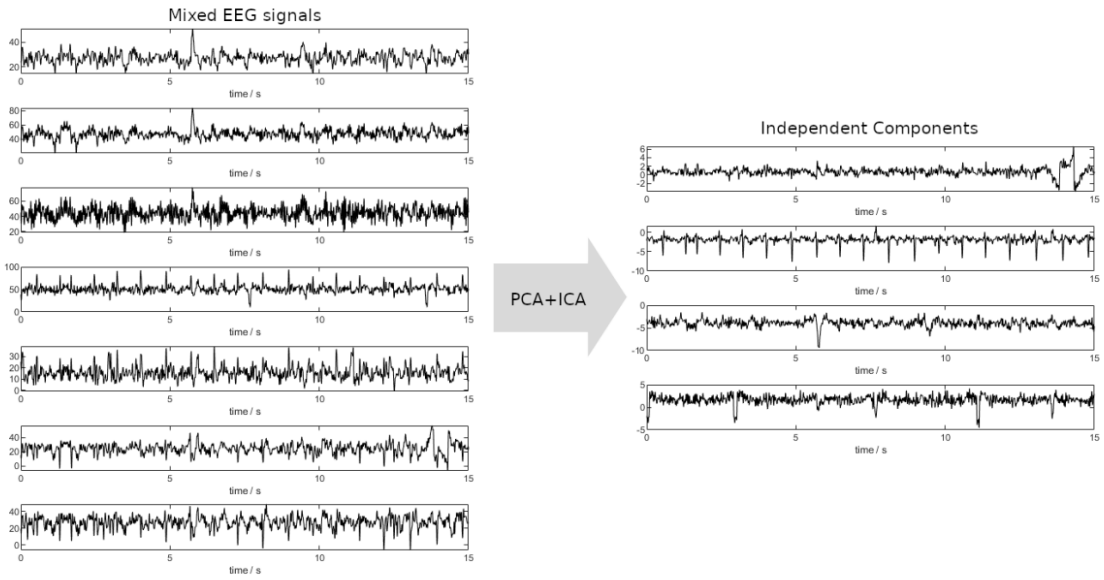

Figure 3. The basic idea of dimension reduction and ICA. From the seven measured EEG signals that were bandpass filtered (left). ICA is able to recover the source signals that were mixed in the measurements (right). For example, cardioballistic component (second IC) can be easily seen as one of the ICs.

Cross-frequency coupling

Studying coupling between different frequency oscillations is n't as straightforward as its with oscillators of same frequency, where direct comparison of phases can be done. Methods under cross-frequency coupling have been developed for problems like these. There are three commonly used methods to assess the coupling between two different frequency bands. Two of which are phase-based techniques: Cross-frequency phase synchrony (CFS) and phase-amplitude coupling (PAC). And the third one which is not phase-based: cross-frequency amplitude-amplitude correlation (AAC).

Cross-frequency phase synchrony is a form of phase synchrony where the stable phase difference takes place between two oscillators with m:n (where m and n are integers, for example 1:2) frequency ratio. It operates at the temporal resolution of the faster oscillation unlike PAC or AAC which are not related to the phase of the faster oscillation [41] and therefore not related to the spike timing of the faster neuronal processing. CFS is quantified by testing whether m:n multiplied phase difference remains stable. In humans CFS has been observed resting state [42] and task-based studies with EEG and MEG [43].

Cross frequency AAC is defined as direct coupling between the two oscillation's amplitude envelopes. Since neither the phase of the slower nor the faster oscillation are related to this technique, the correlations are unrelated to neuronal spike-time relationships. Therefore, AAC cannot express direct integration of processing among the two frequencies but are more likely to reflect co-modulation of excitability between the coupled frequencies. [41]

PAC on the other hand, reflects a third type cross-frequency interaction. It signals the modulation of the faster oscillation's amplitude by the phase of the slower oscillation. It can be quantified by evaluating 1:1 phase synchrony between the phase of slow oscillation and the phase of the slow-filtered amplitude envelope of faster oscillation [15]. PAC has been suggested to underlie cross-frequency integration [44]. It is independent of the phase of the faster oscillation and hence cannot produce consistent temporal and spike-time relationship between the slow and the fast oscillation [43] which are essential in the regulation of neuronal communication [45].

PAC has been observed in animal and human studies with cortical and subcortical structures under variety of conditions and using different measures. Coherent low frequency oscillations seem to also be important part in regulation of large-scale networks. In a way that phase interactions can propagate throughout larger networks due interregional phase locking. These coupling patterns between different brainsites might help binding together anatomically dispersed functional cell assemblies. It is still open what is the relationship between these different coupling mechanisms if there is any. It is also not known whether one type is more general over another. [44]

Transfer entropy

There is a tendency in literature to use relative phase between coupled oscillators to infer which one is the source and a follower. Leading oscillator does not necessarily drive the lagging signal. Therefore, phase-difference alone is not sufficient for determining directionality of coupling and more sophisticated approach is needed. Transfer entropy [46] measures how much information the source process provides about the state transitions in the target. In my case whether knowing the ISF phase lowers the uncertainty or helps to predict future state transitions of the higher EEG activity or vice versa. It is measure of effective connectivity making it able detect directed causal relationships.

In information theory, information itself is defined to be reduction in uncertainty. This uncertainty contained in a non-deterministic dynamic process, in my case the phase relations of ISF and higher frequency EEG-rhythm envelopes, can be quantified using the concept of Shannon's entropy $H(X) = \sum p(x) \log_2(1/p(x)) = -\sum p(x) \log_2 p(x)$. The joint entropy of two discrete variables is given by $H(X,Y) = \sum p(x,y) \log_2 p(1/(x,y))$. Base in the logarithm 2 can be used to express the units in bits. Since entropy reflects likelihood of events, probability distributions are used in the calculations. State space transition or binning of the data is used to produce the discrete probability distributions, where bins are referred as different states.

More concentrated probability distributions have lower entropy, since they contain less 'surprising' events and values are more likely to be in certain states, in contrast to even distributions where equal probabilities are for large number of states and therefore holds high uncertainty about the state of the variable. On the other hand, if variable has only one possible state with likelihood of 1, it has no uncertainty and therefore zero entropy. [47], [48]

Conditional entropy $H(X|Y)$ describes entropy that remains in *X* after given the knowledge of variable *Y*. There exists a relation between conditional entropy and joint entropy of two variables $H(X,Y) = H(X) + H(Y|X)$. Total entropy of *X* must also equal the entropy remaining in *X* after learning *Y* and the information provided by *Y* about *X*: $H(X) = H(X|Y) + I(X;Y)$, where $I(X;Y)$ is also known as mutual information. Due to symmetry of $I(X;Y) = I(Y;X)$ mutual information can be rearranged as $I(X;Y) = H(X) + H(Y) - H(X,Y)$. Mutual information can be extended using joint variables, useful for calculating combined effects of two variables and importantly it can be conditioned by the effect of third variable $I(X;Y|Z) = H(X|Z) - H(X|Y,Z)$. This leads us to transfer entropy which is a special case of conditional mutual information where specific temporal ordering is used. Transfer entropy measures information about future states of Y provided by the past states of X, given information of the past states of Y:

$TE(X \rightarrow Y) = I(Y_{future}; X_{past}|Y_{past}) = H(Y_{future}|Y_{past}) - H(Y_{future}|X_{past}, Y_{past})$. TE can be interpreted as better measure of causality than just $I(Y_{future}; X_{past})$, since TE measures changes caused in Y from X that cannot be explained by the history of Y alone. [47]

Phase TE (PTE) is used in same fashion as real-value TE but is applied to instantaneous phase signals. In the presence of noise and linear mixing, phase TE is more robust estimate than TE and is suitable for large-scale directed connectivity analyses, such as whole scalp EEG [46].

TE and PTE are based on the principle of granger causality and can provide frequency specific information about the connectivity, which is why this metric is well suitable for my analysis [46], [48]. Information flow and causality are closely related but still two distinct phenomena [48]. Causality tells us whether intervention on the source causes effect on the target, whereas information flow describes whether an observation of the source helps predict the phase transitions of the target [48]. PTE requires priori estimate of an analysis lag, however the TE values are not sensitive to the lag and connectivity can be accurately detected over wide range of analysis lags [46].

Methods

Experimental design

The study was approved by The Regional Ethics Committee of the Northern Ostrobothnia Hospital District. A written informed consent was obtained from participants according to the Declaration of Helsinki. Following criteria was used to exclude subjects from the study: Smoking, continuous medication, neurological or cardio-respiratory disease. Thirty subjects were scanned twice, first recording during wakefulness and second after one night of sleep deprivation. Before the recordings, consumption of alcohol or caffeine was prohibited. Sleep scoring was made offline from the EEG recordings by experienced clinical neurophysiologists. Subjects were excluded from the study if they didn't score sleep during sleep deprivation recordings. Recordings were left out also based on insufficient data quality. Final group sizes were 21 awake (average age 29,2 ± 6.8 standard deviations, 8 females) and 21 (28,4 ± 6.3 y, 11f) sleep subjects.

Multimodal imaging setup [49] was used, taking place during fMRI recordings. Two separate recordings were performed for each subject lasting from 10 to 15 minutes. Awake recordings were done after full night of sleep, with eyes open fixating a cross during afternoon. Sleep scans were done in the morning after a night of sleep deprivation. Sleep deprivation has been previously used to effectively get subjects to enter deeper sleep states during the recordings [50], [51].

Full-band EEG was recorded with Electrical Geodesics MR-compatible (GES 400) system, with 256-channel high density net (HydroCel Geodesic Sensor MR net) and DC-coupled amplifier (Net Amps 400). Sampling rate was set to 1 kHz. Electrode 'Cz' was used as a reference channel during recordings. Electrode impedances were inspected before the recordings. Signal quality was further studied by performing test recording with eyes open and eyes closed. In the electrode net, silver-chloride (AgCl) plated electrodes are surrounded by a sponge that were wetted with liquid electrolyte before the recordings to stabilize electrode-skin interface.

Preprocessing

Gradient artifacts arising from switching of the MRI gradients were removed using template subtraction (average artifact subtraction) with Brain Vision Analyzer (v.2.1, Brain Products) [52]. Ballistocardiographic artifacts, related to blood flow in scalp arteries, were also removed using Analyzer's algorithm based on sliding template subtraction, which utilises ECG-signal to find positions of R-peaks of the QRS-complex corresponding to ventricle contraction. After template was fitted visual inspection of R-markers positions was done, to ensure correct positioning. The correction is performed by subtracting average blood pulse curve from each channel independently. Rest of the signal processing steps and analyses were performed in Matlab (v.R2018b-2021a, MathWorks).

All the recordings were segmented in length of 10 minutes to match data lengths. Linear trends were removed to attenuate stable baseline drift caused conductivity change in electrode-skin interface [53], which is known to affect performance of various preprocessing steps. I used FastICA [54] algorithm in combination with PCA dimension reduction (150 components) to transform datasets into independent components, where artificial ICs were identified and removed. The dimension reduction was used since enhanced performance was noticed. Symmetric approach was used, that estimates the components in parallel using the default nonlinearity of $g(u) = u^3$. My main concern was to remove ocular components, which can manifest themselves in the low frequencies, which could interfere the following analysis. Since ocular artifacts can variate in frequency and overlap with other studied frequency bands, conventional frequency domain filters are not suitable. In the awake recordings subjects were instructed to fixate on a cross, which is known to reduce the frequency of eye saccades. To further minimize non-linearities and enhance the performance of ICA, I used spike detection algorithm with amplitude threshold to identify and remove most prominent artificial spikes, arising from example from small movement of the electrode. To keep the recordings intact, I interpolated the trends for the gaps and used data from intact signal to fill the gap as real data imitating injections like is done in inpainting [55]. Bad channels were excluded from ICA and spherically interpolated afterwards. EEG records

signal relative to reference electrode, which was in my case on the center of the head. Since I expected the results to be widespread all over the scalp there are better options. The recordings can be re-referenced afterwards without affecting recordings. There are also reference free solutions such as surface Laplacian, however they are not suitable for studying slow spatial features [56]. Recordings were referenced to linked mastoid electrodes behind ears, which are located near other electrodes but record less brain activity. This referencing preserves as much 'true' signal as possible.

All recordings were sleep scored manually using American Academy of Sleep Medicine guidelines by clinical neurophysiologists who had experience in sleep scoring. Data was categorized in 30s segments into wakefulness and non-REM (N1-N3) sleep. EEG epochs were scored as awake, N1 (light sleep), N2 (intermediate sleep with K-complexes and/or sleep spindles) and N3 (slow wave sleep) (Table 1).

Table 1. Sleep scores for each individual EEG recordings with final group sizes. Sleep was scored in 30 second epochs, where '1-3' indicates non-rem sleep depth, 'w' denotes wakefulness and 'a' for artificial epochs. Each column corresponds to one epoch.

Sleep classifications

Control group	1	2	3	4	5	6	7	8	9	10	11	12	13	14	15	16	17	18	19	20
Subject 1	w	w	w	w	w	w	w	w	w	w	w	w	w	w	w	w	w	w	w	w
Subject 2	w	w	w	w	w	w	w	w	w	w	w	w	w	w	w	w	w	w	w	w
Subject 3	w	w	w	w	w	w	w	w	w	w	w	w	w	w	w	w	w	a	a	a
Subject 4	w	w	w	w	w	w	w	w	w	w	w	w	w	w	w	w	w	w	w	w
Subject 5	w	w	w	w	w	w	w	w	w	w	w	w	w	w	w	w	w	w	w	w
Subject 6	w	w	w	w	w	w	w	w	w	w	w	w	w	w	w	w	w	w	w	w
Subject 7	w	w	w	w	w	w	w	w	w	w	w	w	w	w	w	w	w	w	w	w
Subject 8	w	w	w	w	w	w	w	w	w	w	w	w	w	w	w	w	w	w	w	w
Subject 9	w	w	w	w	w	w	1	w	w	w	w	w	w	w	1	w	w	w	w	w
Subject 10	w	w	w	w	w	w	w	w	w	w	w	w	w	w	w	w	w	w	w	w
Subject 11	w	w	w	w	w	w	w	w	w	w	w	w	w	w	w	w	w	w	w	w
Subject 12	w	w	w	w	w	w	w	w	w	w	w	w	w	w	w	w	w	w	w	w
Subject 13	w	w	w	w	w	w	w	w	w	w	w	w	w	w	w	w	w	w	w	w
Subject 14	w	w	w	w	w	w	w	w	w	w	w	w	w	w	w	w	w	w	w	w
Subject 15	w	w	w	w	w	w	w	w	w	w	w	w	w	w	w	w	w	w	w	w
Subject 16	w	w	w	w	w	w	w	w	w	w	w	w	w	w	w	w	w	w	w	w
Subject 17	w	w	w	w	w	w	w	w	w	w	w	w	w	w	w	w	w	w	w	w
Subject 18	w	w	w	w	w	w	w	w	w	w	w	w	w	w	w	w	w	w	w	w
Subject 19	w	w	w	w	w	w	w	w	w	w	w	w	w	w	w	w	w	w	w	w
Subject 20	w	w	w	w	w	w	w	w	w	w	w	w	w	w	w	w	w	w	w	w
Subject 21	w	w	w	w	w	w	w	w	w	w	w	w	w	w	w	w	w	w	w	a

Sleep group	1	2	3	4	5	6	7	8	9	10	11	12	13	14	15	16	17	18	19	20
Subject 1	w	w	w	w	w	w	w	w	w	w/1	w	1	1	1	2	1	1	2	2	2
Subject 2	1	1	1	1	2	2	1	1	2	2	2	2	2	2	1	1	1	1	1	2
Subject 3	2	2	w	w	1	1	1	2	2	2	2	2	2	2	2	2	2	2	2	2
Subject 4	w	1	1	1	1	1/2	1	1	1	1	1	1	1	1	1	1	2	2	2	1
Subject 5	w	w	w	1	w	w	1	w	1	1	1	w	w	w	w	w	w	1	w	w
Subject 6	w	a	1	1	1	1	2	2	2	1	w	2	2	2	2	2	2	2	2	2
Subject 7	w	w	w	1	1	1	1	2	2	2	2	2	2	2	1	1	2	2	2	2
Subject 8	w	w	w	w	1	w	1	1	w	1	1	1	1	1	1	w	1	2	1	w
Subject 9	1	2	2	2	1	w	1/2	w	1	w	w	1	1	1	1	w	1	1	1	1
Subject 10	2	2	2	2	w	w	w	1	2	2	2	2	2	2	1	2	1	2	2	3
Subject 11	1	1	1	1	1	a	1	2	2	a	2	2	2	2	2	2	2	2	2	a
Subject 12	1	2	a	1	2	a	2	2	2	1	2	2	2	2	2	1	1	2	1	2
Subject 13	w	w	1	1	1	1	w	1	2	2	w	w	w	1	1	w	w	w	w	w
Subject 14	1	w	w	w	w	w	2	2	2	a	1	2	2	2	2	2	1	2	2	2
Subject 15	w	w	1	1	1	2	1	1	2	2	2	1	1	1	w	1	2	2	2	2
Subject 16	1	1	1	1	1	1	1	2	2	1	1	2	1	1	w	1	1	2	1	1
Subject 17	1	1	1	w	w	w	a	1	2	2	w	2	1	2	2	2	2	w	1	1
Subject 18	w	1	1	1	1	1	1	1	1	1	1	1	1	1	1	1	1	1	1	1
Subject 19	w	1	1	1	1	w	w	1	1	2	2	1	2	2	1	1	1	2	1	2
Subject 20	w	1	1	1	2	2	1	1	1	2	2	2	1	1	w	1	1	2	2	1
Subject 21	w	w	w	w	w	1	1	1	1	1	1	1	2	2	1	2	2	1	2	2

Spectral analysis

Time-frequency (TF) spectral analysis was made with wavelet convolution using mirrored time-series to avoid edge effects which occur during temporal filtering especially seen at the lowest frequencies. Mirroring of the signal from both ends generates buffer zones containing the edge effects and can be later cut out. Wavelet convolution can be used to extract frequency specific information about the signal similar to conventional methods like Fourier transform. Unlike Fourier transform wavelet convolution does not require signal stationarity, which long EEG time-series violates. Wavelet convolution also gives temporal specificity due to its nature. Complex Morlet wavelets are sine waves of different frequencies tapered by gaussian. Thanks to Gaussian windowing the wavelets taper to zero at the edges and do not generate artifacts in the filtering process like happens with sharp filter kernel edges. Gaussian windowing also reduces the weight of the surrounding timepoints. Therefore, estimate of power at specific timepoint is also influenced by surrounding timepoints. [56]

Time-domain convolution involves calculation of sliding dot products between filter kernel i.e., the wavelet and the signal. Convolution in time domain is equal to multiplication in frequency domain. Therefore, convolving signal with wavelet in time domain equals multiplying frequency domain signal with frequency domain of the filter kernel and then taking inverse Fourier transform of the results. It is more convenient to calculate wavelet convolution in the frequency domain due to faster calculation. [56]

Wavelet convolution, implemented in frequency domain was performed using complex Morlet wavelets (Eq.1). Logarithmic frequency range between 0.05 and 100 Hz was used, with 70 steps and constant wavelet cycle of 7, which is related to the width of the gaussian by (Eq.2). This parameter controls the trade-off between time and frequency precision in a way that larger number of cycles gives better frequency precision. See (Figure. 5) for more information about wavelet properties. Three pieces of information can be obtained from convolution results: projection onto real axis that is the filtered signal, magnitude of the complex vector that is the amplitude or as squared represents the power, and angle of the vector with respect to positive real axis which is the phase angle estimate. [56]

TF-power estimates were acquired from squared magnitude of the convolution results. Square root of TF-power was further modified into relative amplitude (Eq.3) to reduce subject specific variability in power. I used sleep scores to categorize the epoched power estimates to wakefulness and sleep (N1-N3). I discarded wake epochs of the sleep study and vice versa to gain even more accurate estimate.

Phase-amplitude coupling

Finite impulse response (FIR) Hamming windowed bandpass filters were designed to filter ISF into two separate bands ($ISF_{1\text{-}EEG}$: 0.008-0.05 Hz & $ISF_{2\text{-}EEG}$: 0.05-0.1 Hz) to improve the accuracy of phase-based calculations, since phase is defined only for narrowband signals. Sharp transition in the frequency domain window such as rectangular windowing can generate ringing artefacts. Hamming windowing generates smoother passband frequency response, eliminating the ringing effects [56]. The ISF range of 0.008-0.1 Hz was chosen to obtain maximum coverage, without crosstalk with respiratory frequencies, which can go as slow as 0.1 Hz. Minimum filter kernel length was used i.e., one cycle of the lowest frequency. To avoid edge artifacts occurring in the temporal filtering process, signal was mirrored from both ends. Mirrored time-series $x(n = 1, .., N)$ were zero-phase filtered $x_{ISF}(n)$, which is recursive filtering method that doesn't cause phase distortions or offsets like conventional filtering, especially important with our phase-based calculations. FIR bandpass filters were designed similarly to five higher EEG frequency bands (delta: 1-4 Hz, theta: 4-8 Hz, alpha: 8-13 Hz, beta: 13-30 Hz, gamma: 30-40 Hz) and zero-phase filtered producing signals $x_{High}(n)$. Number of filter taps was increased to 6 cycles of the lowest frequency in each band, to increase stopband attenuation and gain more accurate frequency response. Mirrored signals were segmented back to their original lengths.

PAC is a form of cross-frequency coupling where the phase of the slower rhythm is coupled to the amplitude of the faster oscillation. I used phase-locking value to assess the magnitude of coupling between ISF and fast activity, following methodology from [15], [43], [57]. Hilbert transform was applied, which is done by taking the FFT of the time-series and replacing negative frequency Fourier-coefficients with zeros, then calculating the inverse FFT. Resulting in so called analytical signals $z_{ISF}(n)$ (Eq.4), from which ISF phase time-series were extracted $\theta_{ISF} = arg(z_{ISF}(n))$. For higher frequency bands Hilbert amplitude envelopes were computed by taking complex magnitude of the Hilbert transforms $a(n) = |z_{high}(n)|$. Amplitude envelopes were then filtered to infraslow frequency bands using the same filters as previously mentioned to produce $A_{high}(n)$. After the filtering, signals were downsampled to 3 Hz to speed-up computation, which can be done since PAC operates on temporal resolution of the slower oscillation. Hilbert transform was applied to envelopes $A_{high}(n)$ to extract the instantaneous phase $\theta'_{high} = arg(z_{A_{high}}(n))$. PAC was then quantified as 1:1 phase synchrony between θ_{ISF} and θ'_{high}.

PAC coupling magnitude between time-series was estimated using phase locking value [58] (Eq.5) as stable phase difference over time, giving one estimate of phase synchrony for each channel. It is more suitable for my analysis compared to e.g., coherence since it does not require signal stationary, which long EEG time series violates [58]. PLV is geometrically defined as the length of average complex vector on unit circle that is

obtained from phase difference. PLV of 0 indicates no phase synchrony and 1 represents perfect synchrony. PLV was calculated for each electrode between both ISF bands and faster frequency bands (Figure 4).

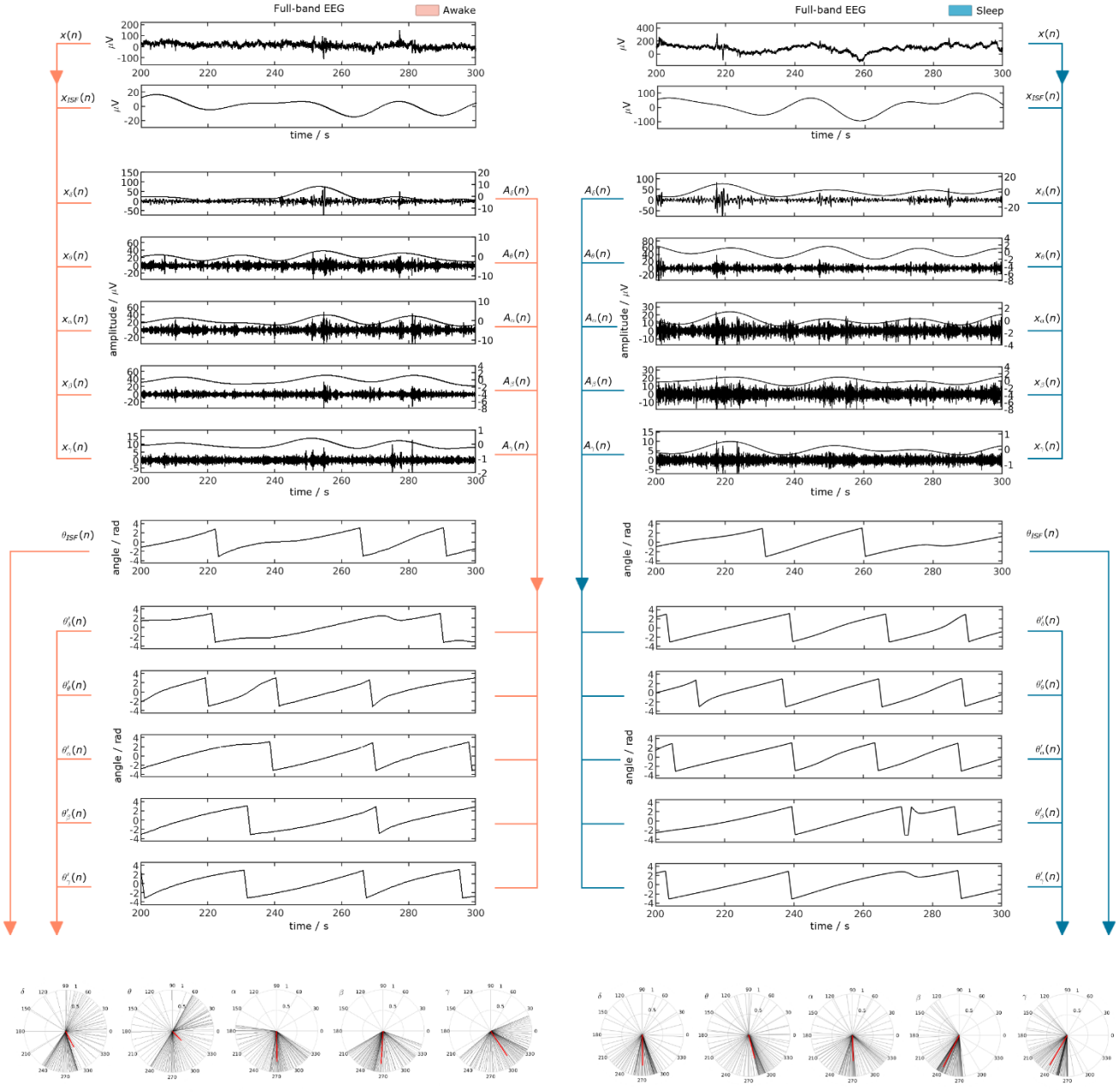

Figure 4. Workflow of the PAC analysis. Arrows represent the calculation ordering. Neural oscillations amplitude envelopes are filtered to corresponding ISF frequencies, whose phases are then compared against the ISF phase time series to calculate PAC. Unit circles are used to visualize the coupling pattern, where the length of the red arrow is PLV, and its direction is the average phase difference.

Respiratory frequency related results were also studied using PAC. Individual respiratory frequencies were calculated from end-tidal CO_2, which records the inhaled and exhaled concentration of CO_2. Short-time FFT is windowed version of Fourier transform where the signal itself is tapered by window function to prevent edge artefacts [56]. This also attenuates valid signal, that can be countered using temporally overlapping segments. The frequency of respiration is captured in end-tidal CO_2, which I calculated using short-time Fourier transform with 50 second Hamming tapered windowing and 50% overlap. Peak of the respiration frequency was then used as a center frequency for complex Morlet wavelet (N=5). Wavelet convolution implemented in frequency domain was then used to filter the EEG recordings in respiratory frequency. First, I compared respiratory frequency EEG ($RESP_{EEG}$) with neural bands. Neural bands were handled similarly as with the ISFs, with an exception that now the fast envelopes were filtered down to respiratory frequency. Furthermore, I compared $RESP_{EEG}$ to ISFs following the same principles.

Properties of the designed Morlet wavelets used in spectral and PAC calculations (Figure 5) were inspected with frequency and time resolution estimates, which were calculated from full width half maximum (FWHM) of each wavelet. As expected, frequency resolution is good at the slowest frequency range and becomes more affected by surrounding frequencies as the center frequency increases when wavelet number is kept constant. Time resolution on the other hand acts reversely where lower frequencies exhibit decreased time resolution.

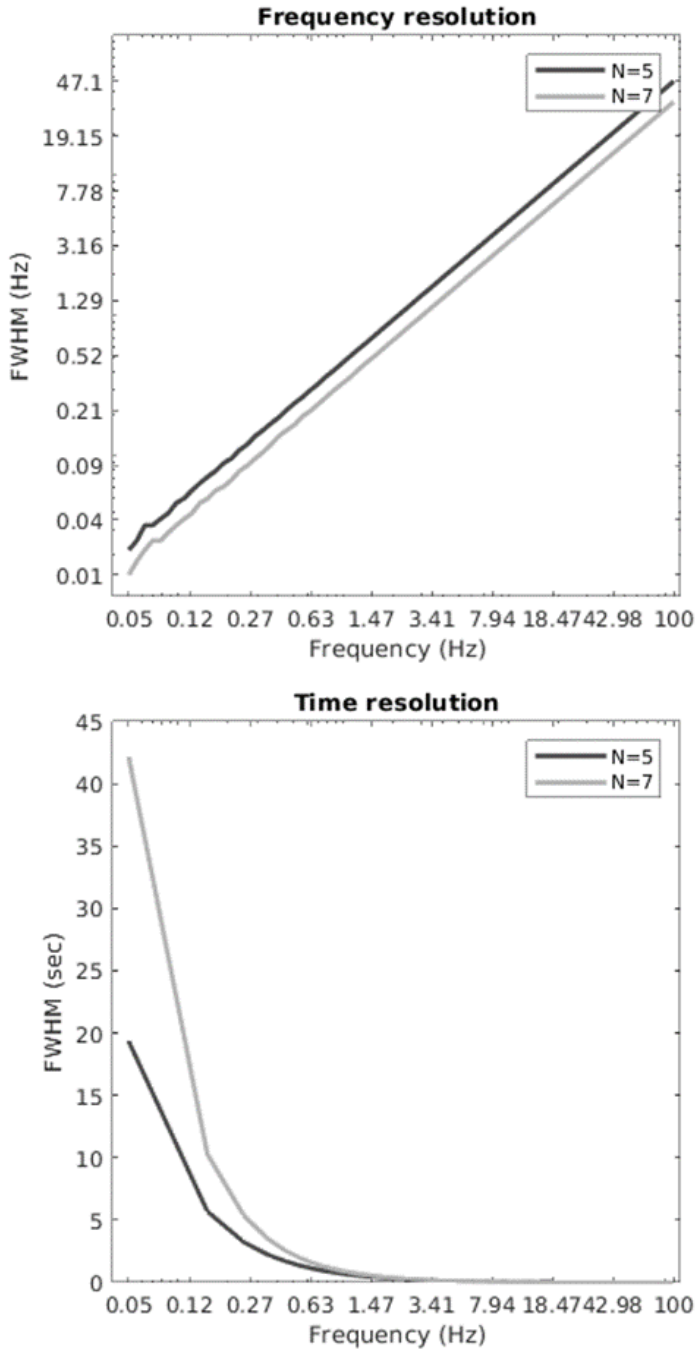

Figure 5. Frequency and time resolution of the designed Morlet wavelets, where N corresponds to number of wavelet cycles. Resolution is interpreted as Full width at half maximum (FWHM) of the wavelets in frequency and time domain. Frequency axes are visualized in logarithmic manner

Phase transfer entropy

Since information encoding, storing, and computing is central behaviour of brain function, I approached the question concerning directionality of the frequency specific interactions from information theory perspective. As causal relationships cannot be defined from correlation analyses or phase synchronization alone, I used phase transfer entropy [46] to assess information flow between phases of slow physiological rhythms and faster neuronal rhythm amplitudes. PTE results tell whether knowing the ISF phase lowers the uncertainty or helps to predict future state transitions of the higher EEG activity or vice versa.

I used previously acquired instantaneous phases θ_{slow} and θ'_{fast} in the following calculations. Sampling rate of 125 Hz was used. Information itself can be quantified as reduction in uncertainty, which can be estimated using Shannon's entropy. State space transition or binning of the data was used to bin the phase time series from -π to π producing discrete probability distributions, from which entropies can were calculated as a summation over all state logarithmic probabilities. Scott's choice [59] was used to estimate the number of bins in state space transition (Eq.6).

For PTE computation (Eq.7) I calculated the probabilities for entropies in equations (Eq.8-10) using script provided by Palva Lab. Base 2 was used in logarithms to express the units in bits [47], [48]. I formulated the PTE values into directional form dPTE (Eq.11), so that sign of the metric tells the information flow direction, or which one of the two studied phase timeseries is the stronger predictor. PTE requires priori estimate of an analysis lag, which I set to one cycle of the slow phase.

Statistical analysis

Null hypothesis power difference distribution (Figure 6a) was built with randomization testing using 10^4 permutations shuffling of the group labels, where the null hypothesis being that vigilance states have same effect on spectral power (two-tailed). Differential power map was then transformed to z-statistics (Eq.12) to determine statistical significance ($p<0.05$). Multiple comparison problem arises when large number of statistical tests are performed. This increases a chance to see an effect that does not exist in reality. Multiple comparison problem was assessed with maximum statistic correction [56], in which the null distribution was built from minimum and maximum values of the permuted maps and statistical significance threshold ($p<0.05$) could be extracted from 2.5 and 97.5 percentiles.

Median PLV were compared groupwise (Figures: 6b left, 8a left, 9a left) using Wilcoxon rank sum test with false discovery rate (FDR) adjustment (Benjamini-Hochberg) [60].

FDR correction allows to control type 1 errors, reducing the number of false positives. I used adjusted p<0.05 as significance criterion. I tested the null-hypothesis: vigilance state has no effect on PAC (two-tailed). For average PLV difference topography (Figure 6c) I permuted subject labels 10^4 times to build null distribution from which the first whitening significance (p<0.05, thresholds 2.5 % & 97.5 %) threshold masks were made. Maximum statistic correction was used to create even more strict significance mask (p<0.05, thresholds 2.5 % & 97.5 %) that was overlayed on top of the first mask to highlight most significant regions.

To assess the significance of the PAC on individual level (Figures: 6b right, 8a right, 9a right), time shifted surrogate data was used [58], [61]. Null hypothesis distributions were built by splitting the phase of time-series $x(t = 1, .., T)$ from a random time-point k into $x_1 = x(1, .., k)$ and $x_2 = x(k, .., T)$ to construct the surrogate timeseries defined as $x_s = [x_2, x_1]$. This approach preserves temporal autocorrelation structure of the data. Shuffling was done 100 times to produce null-distribution of surrogate phase locking values from which p-values were obtained by calculating the number of more extreme surrogate locking values and dividing by the number of permutations. Alpha level was set again as 0.05 %.

I tested whether the median dPTE differs from zero in other words whether net information flow exists to specific direction. One sample sign test with FDR correction was used to adjust p-values with 95 % confidence level criteria (Figures 7, 8c, 9c). Two sample Wilcoxon rank sum test with FDR correction was used to compare the medians between awake and sleep groups (Figures 7, 8c, 9c). Null hypothesis being that the medians of the two are equal (two-tailed). Adjusted p<0.05 was considered significant.

Effect size estimates (η^2) that describe the magnitude of effect relative to sample size (Table 2) were made using z-values according to formula: $\eta^2 = (Z/\sqrt{N})^2$, where N equals total sample size and Z equals Z-statistic [62]. Common interpretation goes: $\eta^2 \approx .01$ for small $\eta^2 \approx .06$ medium $\eta^2 \approx .14$ large effect size.

Collection of formulas

(Eq.1) $$\omega = e^{i2\pi f t} e^{\frac{-t^2}{2\sigma^2}}$$

(Eq.2) $$\sigma = \frac{n}{2\pi f}$$

(Eq.3) $$RA_i = ({}^{A_i}/_{\sum_i A_i}) * 100\%$$

(Eq.4) $$z(n) = x(n) + iy(n) = a(n)e^{i\theta(n)}$$

where n denotes to discrete time variable, $a(n)$ and $\theta(n)$ are the instantaneous amplitudes and phases.

(Eq.5) $$PLV_{ISF,high} = \frac{1}{N}\left|\sum_{n=1}^{N} e^{i(\theta_{ISF}(n) - \theta'_{high}(n))}\right|$$

where N is the number of samples

(Eq.6) $k = \frac{2\pi}{h}, where\ h = \frac{3.5\sigma}{N^{\frac{1}{3}}}$

(Eq.7) $pTE_{x\to y} = H\left(\theta_y(n), \theta_y(n')\right) + H\left(\theta_y(n'), \theta_x(n')\right) - H\left(\theta_y(n')\right) - H(\theta_y(n), \theta_y(n'), \theta_x(n'))$

(Eq.8) $H(\theta_x(n)) = -\sum p(\theta_x(n)) \log_2 p(\theta_x(n))$

(Eq.9) $H\left(\theta_x(n'), \theta_y(n)\right) = -\sum p\left(\theta_x(n'), \theta_y(n)\right) \log_2 p\left(\theta_x(n'), \theta_y(n)\right)$

(Eq.10) $H\left(\theta_y(n), \theta_y(n'), \theta_x(n')\right) = -\sum p\left(\theta_y(n), \theta_y(n'), \theta_x(n')\right) \log_2 p\left(\theta_y(n), \theta_y(n'), \theta_x(n')\right)$

(Eq.11) $dpTE_{x\to y} = pTE_{x\to y} - pTE_{y\to x}$

(Eq.12) $z = \frac{x-\mu}{\sigma}$

(Eq.13) $H\left(\theta_y(n), \theta_y(n')\right) = -\sum p\left(\theta_y(n), \theta_y(n')\right) \log_2 p\left(\theta_y(n), \theta_y(n')\right)$

Results

Transition from wakefulness to sleep increases ISF spectral power

I used power spectral analysis to assess the difference of sleep and awake states in terms of power in the slow and infraslow frequency bands (Figure 6a). In sleep, spectral power was higher in the ISF_{EEG} and $RESP_{EEG}$ frequencies below 0.2 Hz, and conversely, lower in frequencies above 3.6 Hz. Respiratory pulsation peaks were seen at ~0.3 and ~0.2 Hz in awake and sleep, respectively. I did not observe delta frequency 1-4 Hz power increase typical for deeper sleep stages, which was expected, since recorded sleep was mostly light NREM sleep (Table S1). However, the slow delta (0.2-2 Hz) topography showed increased power over most of the brain during sleep, excluding frontal electrodes. In line with my hypothesis, ISF power was increased in sleep over wide areas frontal dominant (at 0.05Hz, ΔRA=-0.730 %, p<0.001, η^2 =0.364).

Sleep increases ISF coupling with cortical rhythms.

To assess the phase relationship and correlation between the ISF phase and the amplitudes of fast oscillations, I used the PLV based phase-amplitude coupling estimator [15] that enables the isolation of PAC effects attributable to distinct ISF frequencies in the amplitude time series.

Since phase locking is property of narrowband signals, ISF was studied in two separate frequency bands ($ISF_{1\text{-}EEG}$: 0.008-0.05 Hz & $ISF_{2\text{-}EEG}$: 0.05-0.1 Hz). I found that PAC

between the phase of $ISF_{1\text{-}EEG}$ and the amplitude of all faster rhythms was greater during sleep than during awake (Figure 6b, left). This difference between groups was noticeably strongest with alpha band, where an increase of ~0.1 in the median PLV was observed. Significant group differences in PAC were found between $ISF_{1\text{-}EEG}$ phase and delta (ΔPLV=-0.029, p_{adj}=0.031, η^2=0.179), alpha (ΔPLV=-0.081, p_{adj}=0.002, η^2=0.339), and beta (ΔPLV=-0.023, p_{adj}=0.037, η^2=0.142) amplitudes, where differences were focused on central brain regions (Figure 6c). Theta and gamma bands showed similar behaviour, where phase locking was stronger during sleep. PLV compared with surrogate data followed same pattern as raw phase locking values (Figure 6b, right). During wakefulness the number of significantly coupled channels was clearly lower so that 5-15 % of electrodes had significant phase-amplitude coupling effects, compared to 5-35 % in sleep.

To investigate how coherent the phase differences were spatially, I estimated the probability distributions of the average phase differences combined from all frequency bands (Figure 6d) between the $ISF_{1\text{-}EEG}$ and amplitudes of fast oscillations. During wakefulness I found that the phase differences were distributed in a relatively uniform manner. However, in sleep the pattern changed drastically, with heavy tendency towards phase differences around $\pi/2$. Topographical analysis showed that these changes were focused on parietal, central and frontal electrodes.

I found that while infraslow EEG fluctuations are significantly coupled to the amplitude dynamics of fast neuronal oscillations during both awake and sleep states, this relationship is both stronger and anatomically more widespread during sleep.

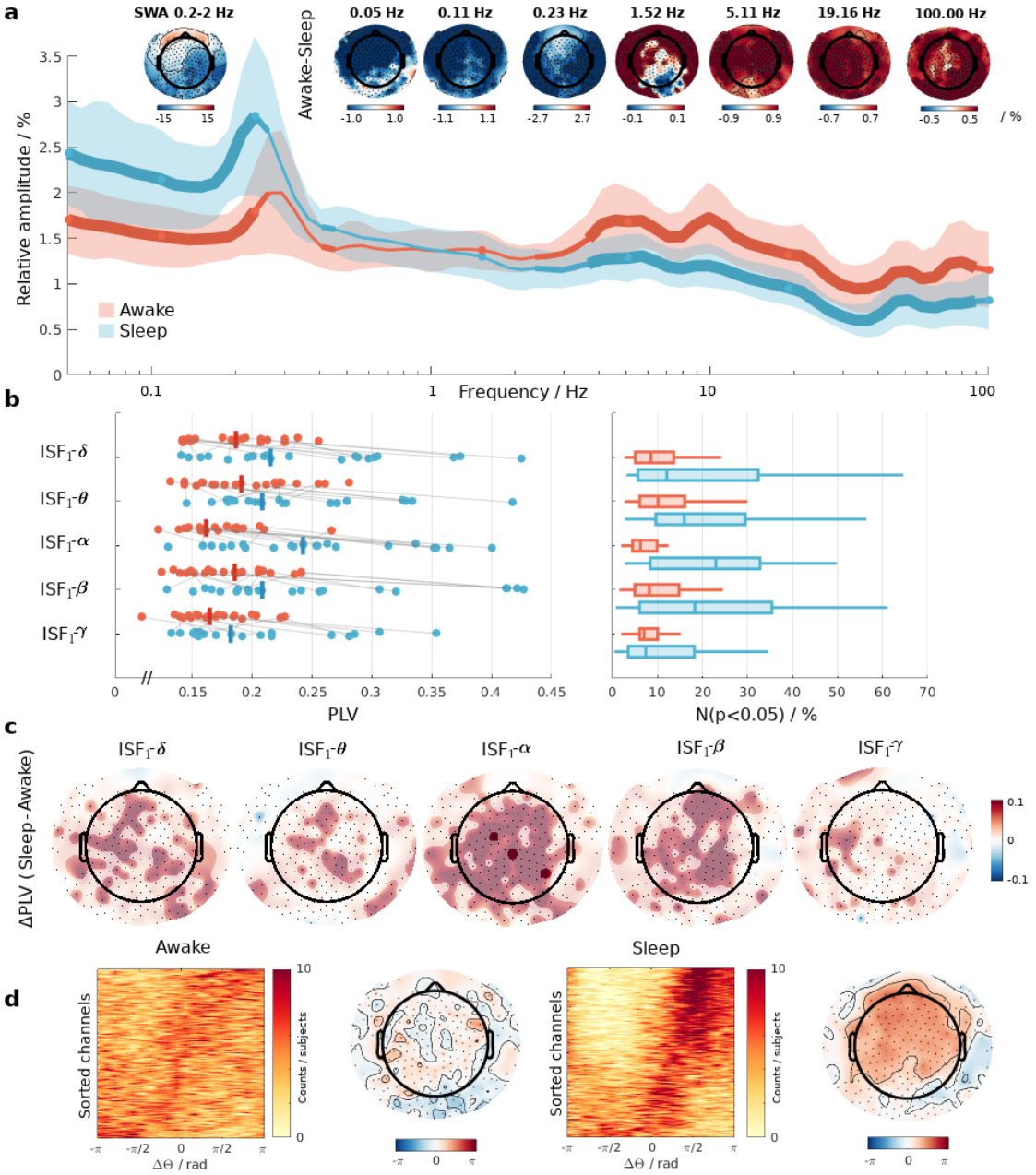

Figure 6. EEG average spectral power & standard deviations are visualised using relative amplitude on a logarithmic scale. The width of the solid lines represents statistical significance at specific frequency in rising order: no statistical significance, permutation tested, permutation test + maximum statistics correction. Topography plots the relative power difference at chosen frequencies. b) Left: Median PLV taken over electrodes, where asterisks indicate statistically significant (adjusted p<0.05) difference in the coupling strength (2-sample). Gray lines connect paired subjects. Right: Number of significantly coupled electrodes in percentiles. c) Difference in average PLV combined with two overlayed whitening masks (p<0.05) and maximum statistics

correction ($p<0.05$). d) Probability estimates of the average phase difference between ISF phase and faster rhythms phase. Channels on the y-axis are sorted to ascending order following the median phase difference. Topographical plot shows the median phase difference taken over the five bands and subjects.

ISF phase drives electrophysiological brain rhythms

The question still unanswered was whether $ISF_{1\text{-}EEG}$ are modulating cortical oscillations or just phase synchronized. To measure this kind of effective or directional phase correlations, I estimated phase transfer entropy (PTE) [46] between the phase of ISFs and the phase of infraslow frequency filtered amplitude envelope of fast oscillations.

I found significant non-zero directional PTE (dPTE) in all frequency bands during both awake (combined *dPTE*: 0.099 bits, $p_{adj}<0.001$ for all bands) and sleep (combined *dPTE*: 0.052 bits, $p_{adj}<0.001$ for all except gamma $p_{adj}<0.05$) states. Importantly, the phase of $ISF_{1\text{-}EEG}$ was a stronger predictor of the fast brain rhythms than vice versa, which implies that $ISF_{1\text{-}EEG}$ significantly drive the amplitude dynamics of fast oscillation (Figure 7). Median dPTE was consistently stronger in awake than in sleep state (average difference 0.047 bits, $p_{adj}<0.02$ and $\eta^2>0.16$ for all bands), with little variation in magnitude of dPTE between frequency bands or scalp topographies.

These findings constitute the first evidence for ISFs driving cortical brain rhythms during both wakefulness and sleep.

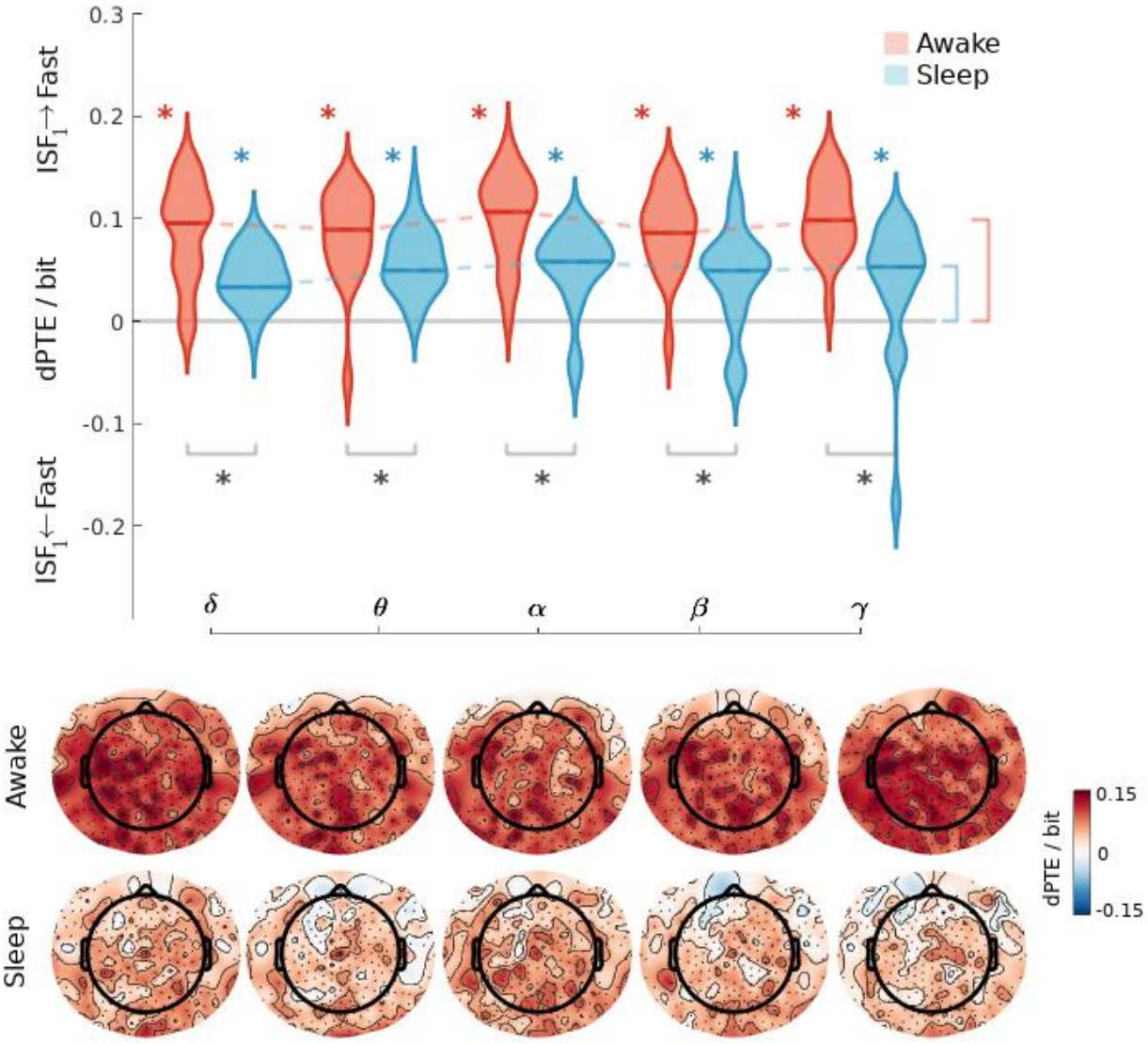

Figure 7. Information transfer between ISF_1 phase and faster rhythms. Top: Probability density estimate of the average dPTE. Since dPTE is a directional metric, the direction of the information flow changes on a sign change. Greek letters indicate the neural band in question. Asterisks indicate statistical significance (adjusted $p<0.05$). Coloured asterisks are for one sample tests, indicating whether there is significant non-zero information transfer. Black asterisks are for 2-sample test. Bottom: Topography shows average dPTE for wakefulness and sleep.

Influence of EEG respiratory frequencies to cortical excitability

We have recently found that respiratory brain pulsations in magnetic resonance encephalography BOLD signals are accompanied by widespread electrophysiological changes. This and evident power peaks seen at respiratory frequencies (Figure 6a) led us asking whether also the respiratory rhythm is phase-amplitude coupled with neuronal oscillations. I repeated same analysis as with ISF to evaluate PAC using individual respiration frequency ($RESP_{EEG}$).

PAC phase locking values between $RESP_{EEG}$ and higher bands (Figure 8a) were marginally lower than seen with $ISF_{1\text{-}EEG}$. On average, I found the PAC to be stronger during wakefulness (mean *PLV*=0.185) compared to sleep (mean *PLV*=0.167). However, differences in PLV magnitudes were small and no significant differences were seen between the two arousal states. PLV compared against surrogate data revealed that $RESP_{EEG}$ coupling to neural amplitudes is widespread phenomenon. Awake state showed interquartile range of significantly coupled channels from 15 to even 80 percent. With sleep in contrast, the same metric varied from 15 to 60 percent.

As before, to further investigate directionality of the phase interaction I calculated dPTE. I found robust directional phase correlation between $RESP_{EEG}$ and faster brain rhythms (Figure 8c) occurring at every tested frequency except for delta rhythm during wakefulness, which were not altered by sleep. The coupling was directed also so that slower $RESP_{EEG}$ predicts the faster neural rhythms both during wakefulness (combined *dPTE*: 0.049 bits, p_{adj}<0.002 for all, except for delta p_{adj}=0.189) and sleep (mean *dPTE*: 0.085 bits, p_{adj}<0.002, except for delta p_{adj}<0.05). Topographical mapping clearly separates frontal electrodes and rest of the scalp where differences take place.

I wanted to see whether there was interaction between ISF_{EEG} and $RESP_{EEG}$. and found, increased coupling during sleep with slower ISF band (Figure 8a). Comparing against surrogate data revealed that this coupling is not widespread, taking place only around 10 % of electrodes. I still found non-zero dPTE directed from $ISF1_{EEG}$ to $RESP_{EEG}$ which indicates that slower ISF is also predicting respiratory frequencies but only very locally (Figure 8c). During sleep the ISF drive of respiratory frequencies dropped significantly, which was seen all over scalp except at some frontal electrodes.

These results confirm that respiration couples with cortical rhythms even on a larger scale than $ISF_{1\text{-}EEG}$. I further showed that respiration also drives neural amplitudes, but interestingly, sleep didn't influence neither coupling strength nor directionality of this interaction, even though respiration frequency became slower and more powerful in its EEG effects (Figure 8b).

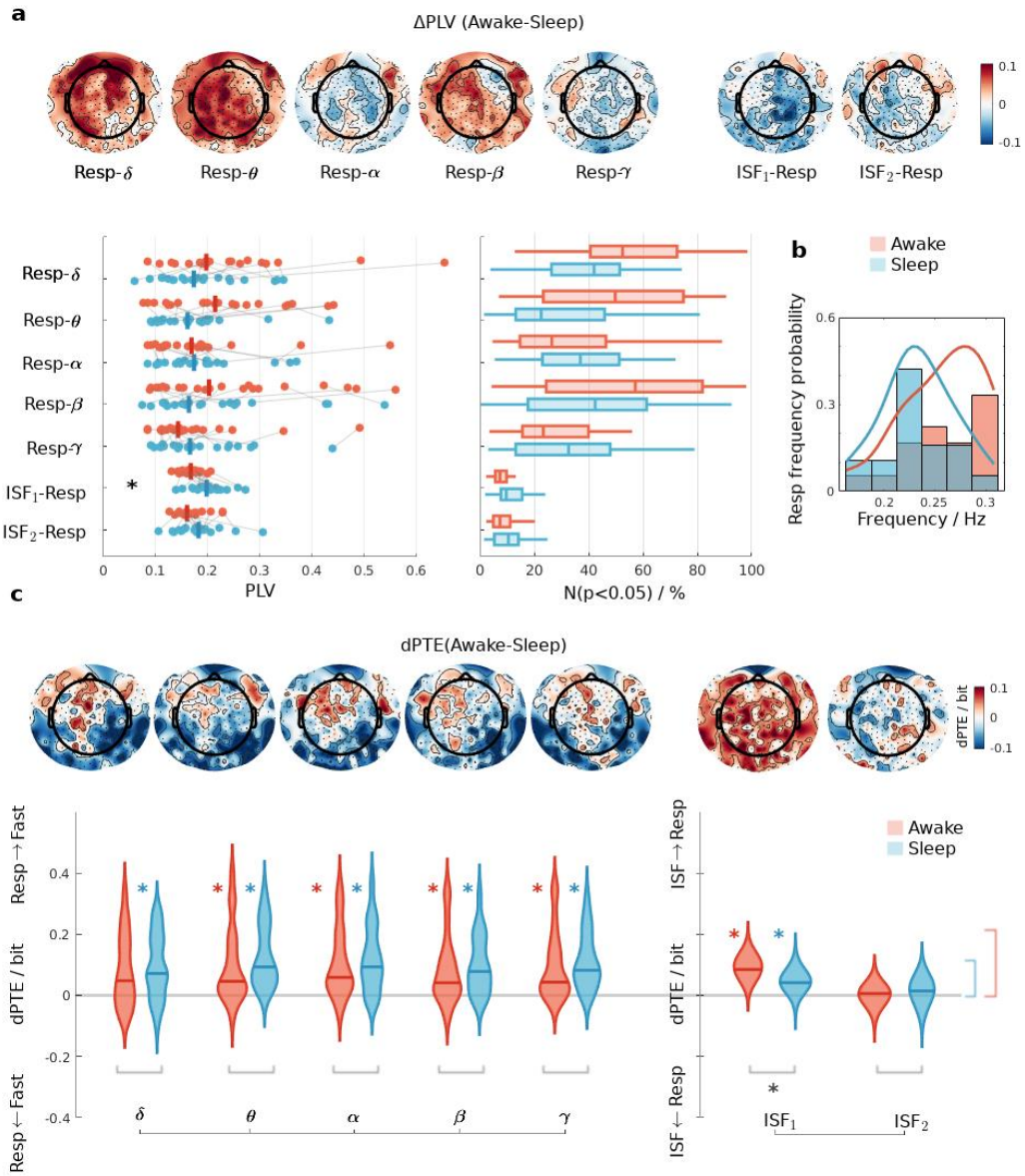

Figure 8. EEG respiratory frequency PAC and dPTE. a) Median PLV of the coupling. Lines on the scatter plot display median for the group. Note that coupling is also tested between ISFs and EEG respiratory frequencies. Topography is the average difference (awake-sleep) in phase locking value. b) Probability estimates of the individual respiratory frequencies. Respiratory frequency for each test subject was taken from capnography which was simultaneously recorded. c) Probability density estimates of the average dPTE. On the left side information transfer between EEG respiratory frequencies and neural frequency bands. On the right side dPTE between ISFs and EEG respiratory frequencies. Topography shows median difference between the groups. Asterisks indicate statistical significance (coloured: 1-sample, black: 2-sample).

Faster ISF_2 phase is not involved in drive of cortical amplitudes

I repeated same analysis pipe for faster $ISF_{2\text{-}EEG}$ (0.05-0.1 Hz) as with $ISF_{1\text{-}EEG}$ band to see if the coupling and directionality with neuronal rhythms stays unchanged. I found similar phase-amplitude coupling patterns with $ISF_{2\text{-}EEG}$, where during sleep the coupling was stronger throughout all the frequencies (Figure 9a left). However, PAC magnitudes were generally lower than with $ISF_{1\text{-}EEG}$. I found significant difference between the two states only with ISF_2-beta coupling (ΔPLV=-0.021, p_{adj}=0.037, η^2=0.142). Comparison with surrogate data (Figure 9a right) confirmed that not only the coupling magnitudes, but also number of significantly coupled electrodes were lower in this faster ISF range. Interquartile ranges of significant PAC electrodes were from 5 to 20 percent, varying between frequency bands. Especially sleep state showed decrease in the extent of coupling. Average phase difference probabilities (Figure 9b) showed a little emphasis on small phase differences. With sleep phase differences from 0 to π were more dominant occurring at frontal electrodes.

In contrast to $ISF_{1\text{-}EEG}$ I found reversed directionality of the phase interaction to occur with $ISF_{2\text{-}EEG}$, directed from fast activity to slow $ISF_{2\text{-}EEG}$ phase (Figure 9c), which I found to be significant during wakefulness with all but beta frequency band (combined dPTE: -0.028, p_{adj}<0.03 for all, except for beta p_{adj}=0.07). Still, I didn't observe significant differences between the two groups.

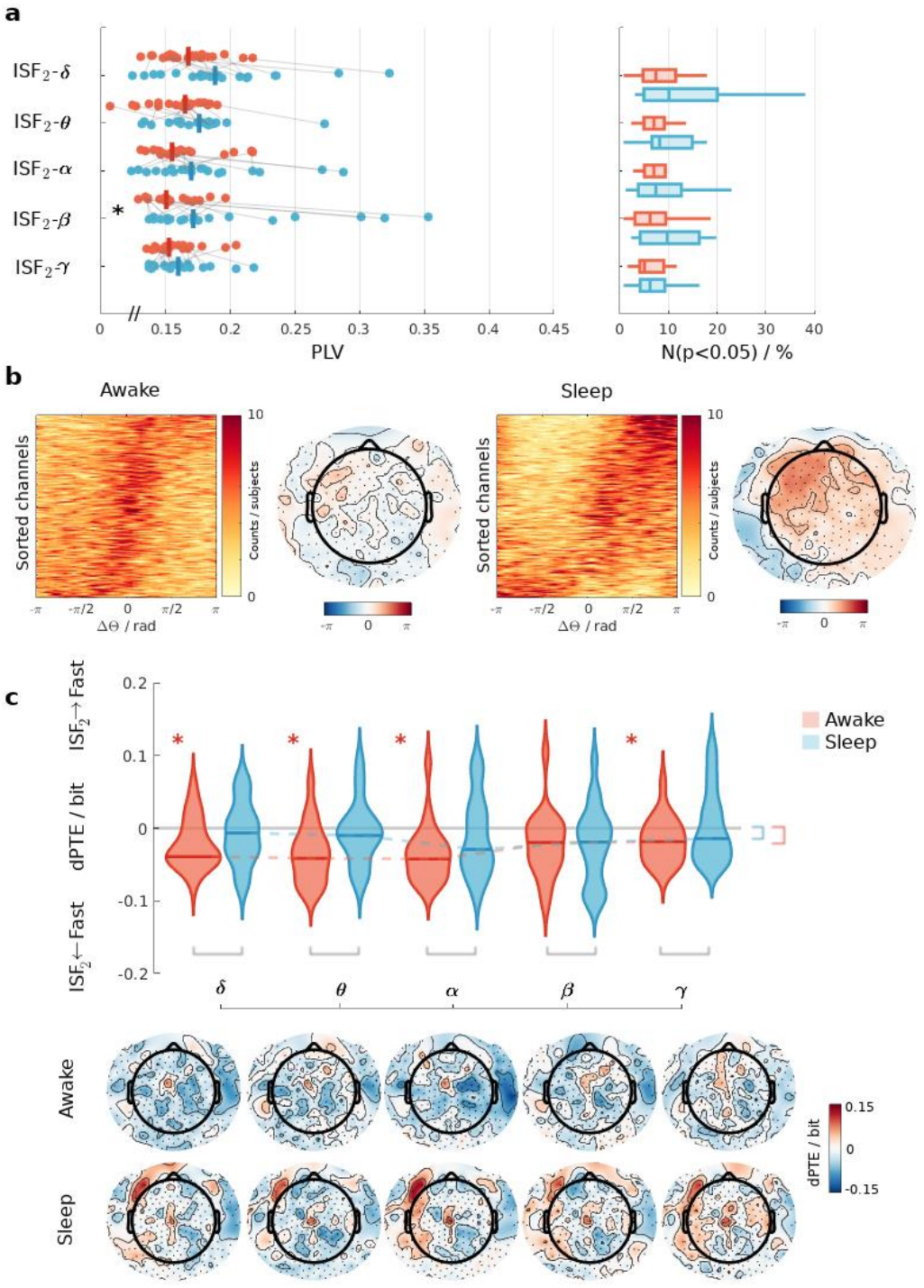

Figure 9. Coupling and information transfer with ISF_2. Panel a) left: Median PLV taken over electrodes. Asterisks indicate statistically significant (adjusted p<0.05) difference in the coupling strength between the two states. Gray lines connect paired test subjects. Right: Number of significantly coupled channels in percentiles. b) Probability estimates phase difference between

ISF and faster rhythms phase. Channels on the y-axis are sorted to ascending order following the median phase difference. Topographical plot shows the median phase difference taken over the five bands and subjects. Panel c: dPTE between ISF phase and faster rhythms. Top: Probability density estimate of the average dPTE. Greek letters indicate the neural band in question. Asterisks represent statistical significance (adjusted $p<0.05$). Coloured asterisks are for one sample tests, indicating whether there is significant non-zero information transfer. Black asterisks are for 2 sample tests i.e., groupwise comparison. Bottom: Topographical presentation for average dPTE for wakefulness and sleep.

Groupwise dPTE differences are not explained by increased autocorrelations

Increased spectral power of the very low frequencies during sleep indicates in the direction of increased autocorrelations. This would make comparison of the two arousal states invalid since increase in autocorrelation leads to decrease in dPTE. I used information theory replicate of autocorrelation (Eq.13) to calculate autocorrelations with the same analysis lag used in the PTE calculations (Figure 10). If the autocorrelations between the wakefulness and sleep differ significantly, it is not meaningful to compare the PTE between conditions. Average was taken over channels and Wilcoxon rank sum combined with FDR correction was used to assess statistical significance, with null hypothesis being that the medians of the two distributions are equal. No significant differences were seen between the groups, meaning that comparison of dPTE values on group level can be made and that correlation differences do not explain the differences observed with phase transfer entropy.

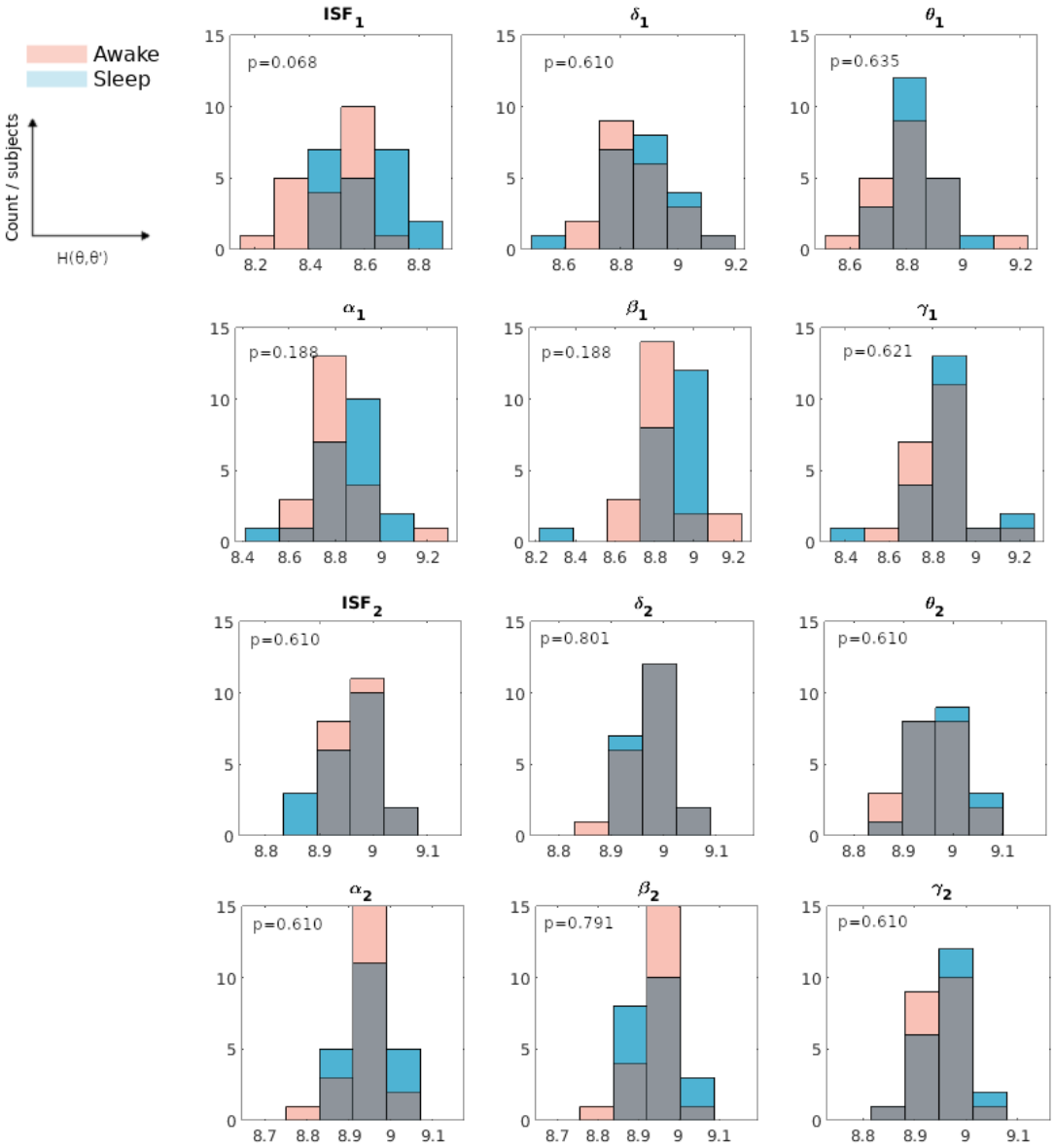

Figure 10. Differences in phase TE are not explained by differences in autocorrelations. First two rows visualise slower ISF_1 (0.008-0.05 Hz) band and related faster neural frequencies, and lower two rows correspond to the faster ISF_2 (0.05-0.1 Hz) band and related bands. X- and y-axis correspond to autocorrelation and histogram count respectively. Greek letters represent slow filtered amplitude envelopes used in PAC and PTE calculations. P-values are FDR adjusted p-values.

Relation between PAC and PTE

I wanted to test if there exist correlation between PAC values measured by PLV and dPTE magnitude. I hypothesized that increased phase-amplitude coupling is accompanied by increased directional PTE, which has been seen with Kuramoto models [63], however

not always [64]. I took median over subjects and combined all five cortical bands in one. I used linear regression analysis using ordinary least squares fit (Figure 11). Coefficient of determination (R^2) between the model and observations were low, therefore linear model was not sufficient to explain variation in the observations. Residuals and residual autocorrelations showed that model was not biased and contained no autocorrelation of residuals.

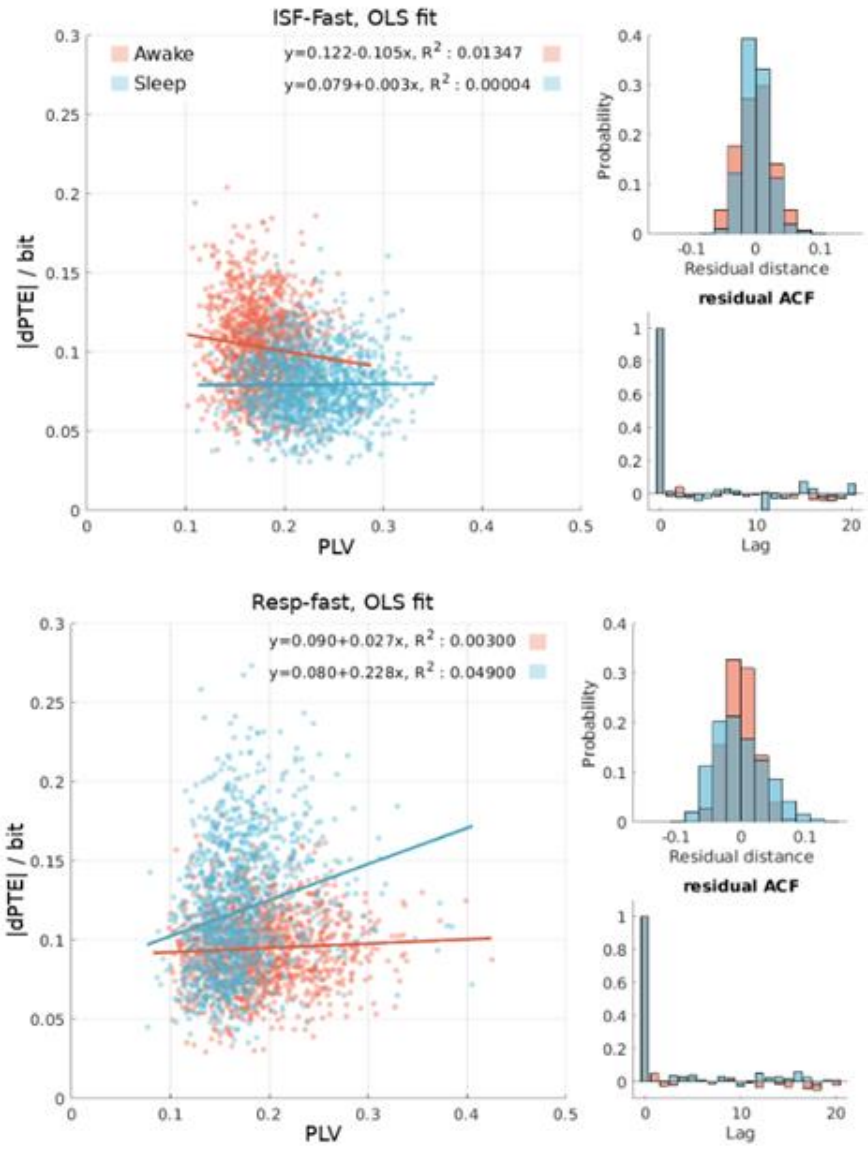

Figure 11. Magnitude of information transfer as a function of PAC strength for ISF_1-neural (top) and $RESP_{EEG}$-neural (bottom) coupling. Ordinary least squares (OLS) fits are marked by solid lines. Histogram and box plot represents OLS residual distances and autocorrelation function respectively.

Table of statistical tests

Table 2. Table of statistical tests. Median PLV and dPTE are shown including adjusted p-values and effect sizes for 1- and 2-sample tests. Red and blue colors mark awake and sleep states respectively.

		Alpha	Beta	Theta	Delta	Gamma
PLV	ISF_1	0.161	0.185	0.191	0.186	0.164
	ISF_2	0.155	0.150	0.165	0.167	0.152
	ISF_1	0.242	0.208	0.208	0.215	0.182
	ISF_2	0.170	0.171	0.176	0.188	0.160
2-sample p_{adj}	ISF_1	0.002	0.037	0.111	0.031	0.185
	ISF_2	0.164	0.037	0.164	0.069	0.563
Eff. Size η^2	ISF_1	0.339	0.142	0.080	0.179	0.046
	ISF_2	0.054	0.142	0.058	0.106	0.008
dPTE	ISF_1	0.110	0.090	0.093	0.099	0.103
	ISF_2	-0.039	-0.016	-0.038	-0.035	-0.016
	ISF_1	0.062	0.053	0.052	0.038	0.054
	ISF_2	-0.026	-0.015	-0.005	-0.003	-0.012
2-sample p_{adj}	ISF_1	0.003	0.003	0.018	0.003	0.001
	ISF_2	0.217	0.960	0.051	0.218	0.349
Eff. Size η^2	ISF_1	0.271	0.259	0.163	0.243	0.376
	ISF_2	0.049	6.03E-05	0.111	0.044	0.024
1-sample p_{adj}	ISF_1	4.77E-06	5.25E-05	5.25E-05	4.43E-04	4.77E-06
	ISF_2	0.002	0.078	0.010	0.030	0.030
	ISF_1	0.001	0.004	9.54E-06	1.05E-04	0.014
	ISF_2	0.426	0.426	0.426	0.664	0.426

		Alpha	Beta	Theta	Delta	Gamma
PLV	Resp	0.169	0.202	0.214	0.197	0.143
	Resp	0.173	0.163	0.161	0.173	0.166
2-sample p_{adj}	Resp	0.546	0.546	0.291	0.291	0.511
Eff. Size η^2	Resp	0.009	0.009	0.070	0.056	0.020
dPTE	Resp	0.060	0.041	0.047	0.051	0.048
	Resp	0.096	0.080	0.093	0.073	0.084
2-sample p_{adj}	Resp	0.597	0.597	0.597	0.597	0.597
Eff. Size η^2	Resp	0.007	0.007	0.047	0.008	0.023
1-sample p_{adj}	Resp	4.43E-04	4.43E-04	0.002	0.189	0.002
	Resp	0.002	4.43E-04	2.10E-04	0.030	4.43E-04

		ISF_1	ISF_2
PLV	Resp	0.167	0.160
	Resp	0.197	0.182
2-sample p_{adj}	Resp	0.008	0.349
Eff. Size η^2	Resp	0.251	0.039
dPTE	Resp	0.089	0.009
	Resp	0.046	0.017
2-sample p_{adj}	Resp	2.70E-05	0.125
Eff. Size η^2	Resp	0.451	0.056
1-sample p_{adj}	Resp	3.81E-06	0.078
	Resp	4.20E-05	0.078

Discussion

Sleep is known to induce changes in the scalp EEG since the discovery of slow sleep related delta waves. It is not until recently that frequencies < 1 Hz has started to reveal their importance in electrophysiological processes. My study showed that infraslow frequency powers increase with concurrent drop at most neural rhythms during NREM light sleep. Changed respiration patterns during sleep were also reflected into the EEG. I found that slow physiological oscillations, i.e., ISF_{EEG} and $RESP_{EEG}$ both reflect gross cortical excitability, especially seen during sleep. I further showed that the two are both not only coupled but predicting neuronal oscillations implying causal relationship and that the two are coordinating and driving faster oscillation amplitudes.

Cortical excitability is driven by ISF

It has been shown previously that cortical ISF reflect neural fast amplitudes, or gross cortical excitability, seen during sleep [15], [30]–[32]. I used same approach in my study with the same metrics to fully evaluate the increased ISF phase correlation with cortical amplitudes comparing sleep against awake resting-state recordings. Most evident increase in PAC was seen in the same alpha, beta, and delta bands. This was the first high density EEG study to quantify the spatial extent and directionality for ISF modulation of cortical neuronal rhythms over the human brain.

In addition, I showed that during sleep the phase difference of the PAC unifies around $\pi/2$ seen especially in frontal areas (Figure. R1d). This might suggest more uniform modulation of the whole brain. During sleep connectivity between cortical nodes is known to collapse, which is reflected as decoupling between cortical oscillations [65]. Could this decoupling of the cortical oscillations be balanced by uniform increase of ISF coupling seen in my study?

Signal crosstalk arising from volume conduction is major limitation in scalp EEG [66]. The ability to consider shared history and common external driving influences between two processes makes the PTE a versatile approach in comparison to PLV along with directionality of the measure [48]. As a nonlinear measure, PTE it is also model free. Therefore, no assumptions about the interaction are needed and it is therefore suitable for explorative analysis such as ours.

In my original hypothesis I stated that ISF serves as driver of the process and this drive should increase during sleep. The phase -interaction was indeed directed from the ISF to neural rhythms both during wakefulness and sleep. This combined with previous

result further strengthens my hypothesis that ISF are orchestrating cortical excitability now measured with two different metrics. I expected the net information flow to be stronger during sleep compared to wakefulness due to clearly increased ISF coupling and power during sleep. Surprisingly, the opposite was found with all tested frequencies. My initial though was that stronger coupling transfers less information due to more constant phase difference. To test this, I quantified the relationship between PLV magnitude and information transfer and found only weak linear correlation between the two (Figure 11) which did not explain the results.

Typically, increased coupling points to direction of increased information transfer, this is however not the case in all systems [64]. Also, with oscillators that are fully phase locked there cannot be any information transfer. Kuramoto models can be used to study effects of synchronous behaviour. It is a model containing a set of coupled oscillators with properties similar to neural populations such as natural frequency and coupling strength, which can be seen as natural firing rate of neuron and degree of excitation and inhibition [67].

Studies with Kuramoto models have shown that information transfer drops significantly before coupled signals reach perfect synchronization [63]. It is thus possible that reduced information transfer I observed during sleep was an indication of stable state prior to synchronization, where information is not as actively transferred, which was supported also by increased phase locking. Furthermore, spectral power increase at ISF could indicate elevated autocorrelations and in theory reflect as a change in PTE. This was tested and the effect was not large enough to be considered significant (Figure 10). I hypothesize that there could be bi-directional phase interaction which takes place during sleep where the driving dynamics interchange, having a cancelling effect on the net dPTE. To verify the previous two possible explanations, analysis which studies coupling strength and directional PTE as a function of time would be needed.

$ISF_{2\text{-}EEG}$ resembles $ISF_{1\text{-}EEG}$ in its PAC effects with neuronal oscillations, but the phase-correlations were much lower along with the extent of the effect. Furthermore, the directionality of the interaction on average seemed to be reversed, implying different source of signal. It's possible that the underlying ISF effect takes place on wider frequency band than studied, overlapping with ISF_2 frequency range or due to spectral leakage, the ISF_2 measures partially the same effect as ISF_1 possibly explaining the similarities between the two. From these results I can surely say that ISF_2 does not modulate cortical rhythms. My observations showed that careful assessment of ISF bandwidth choice needs to be made, due to drastically different results and varying ISF range used in literature.

Respiratory oscillations are active drivers during both arousal states

Clear spectral peak found at the respiratory frequencies along with concomitant fMRI findings and existing literature made us to further explore whether respiration could in fact influence neurophysiological rhythms directly or indirectly by affecting the ISF drive. There is recent evidence indicating that intracranial respiratory pulsations mediated by CSF/venous pulsations could also affect scalp EEG [68]. Recent study with awake mice revealed that respiration-entrained oscillation pattern is coupled and pacing electrical oscillations in the prefrontal cortex [16]. One could argue these to be due to respiratory related motion of the head. Topographical distribution of my results speaks against that measured respiratory frequency oscillations arise from movement of the head as I would expect them to highlight posterior electrodes, which is the most prone area to electrode movement, since the subjects are lying on a bed. Strong respiratory brain pulsations also have been detected in human brains as well using both ultrafast fMRI [68]–[70] and intracranial needle electrode EEG [71], [72] recordings.

My novel finding showed that amplitudes of neural frequency bands, which reflect cortical excitability, were also driven by respiration related $RESP_{EEG}$ phase and not exclusively by $ISF_{1\text{-}EEG}$ phase. Interestingly, unlike with ISF, the phase locking magnitudes and dPTE were not altered by sleep. Sleep increases respiratory power practically in the same areas as slow wave (0.2-2 Hz) power over nearly the whole brain excluding the frontal areas (Figure 6a). Interestingly, sleep induced change in respiration frequency doesn't influence coupling metrics, suggesting stable function of respiration throughout different arousal states.

Electrohydrodynamic changes over the BBB during sleep

The glymphatic model states that the interstitial brain water dynamics between interstitial and perivascular space alters in sleep such that the interstitial space widens, and electrolyte concentrations drop with subsequently lower neuronal excitability. This was experimentally shown as artificial CSF flushing of the brain tissue elicits locally sleep like slowing to slow wave activity while most of the brain was awake with faster EEG activity [73]. And conversely also electrophysiological awake state was introduced during sleep by narrowing the interstitial space and increasing of electrolyte concentrations locally. In my study I saw increased slow and infraslow EEG power over posterior regions during NREM human sleep (Figure 6a), which could possibly inversely mark the areas of increased CSF movement.

As the vasomotor and respiratory pulsations are the two main drivers of both blood flow and CSF in the cortex [74] their role in electrohydrodynamic driving mechanisms needs to be more thoroughly investigated. The glymphatic clearance has been shown to be deteriorated in several major brain diseases ranging from acute trauma and stroke to slow degenerative diseases like Alzheimer's disease, which is thought to be related to

impaired clearance amyloid β proteins [75]–[77] and epilepsy that is accompanied by BBB leakage [78]–[80]. Proper function of the clearance is crucial for neurotoxic proteins to be able to enter paravenous spaces and further to lymphatic vessels. As fbEEG ISFs reflect BBB permeability [6], [14] they could prove to be important part in studying such diseases.

Sleep deprivation is commonly used method to study sleep with limited recording times. In my case the recording time was limited due multimodal imaging including MRI with limited sequence lengths for example. The main time limitation with EEG is however the drying of the electrolyte solution used with wet electrodes. Sleep deprivation however have its disadvantages. Mouse models have shown that continued sleep restriction lasting six days downregulates expression of tight junction proteins at BBB and increases its permeability [81]. Ultimately this can lead to impaired AQ4 channels, which facilitate the CSF flow, followed by dysfunction of the glymphatic system [10], [82]. There is no evidence that one night of sleep deprivation used in my study could have such extreme effects. Recently it was shown that one night of sleep deprivation increases the amount of metabolites in human brain [83]. This implies higher need for clearance the night following, which could have an amplifying effect compared to normal sleep.

Future works remains to be done, whether the ISF phase interactions with cortical rhythms are changed with such neurodegenerative brain diseases. The question left open was why exactly ISF drive was stronger during wakefulness when the phase synchronization was stronger during sleep, more accurate analysis in the time domain could be used to answer these questions. Source-level analysis requiring solving of inverse and forward problems would be useful for more precise localisation of the coupling interactions since scalp EEG signal is prone to volume conduction resulting in spatial imprecision and linear mixing of the scalp signal.

References

[1] C. W. Erwin, E. R. Somerville, and R. A. Radtke, "A review of electroencephalographic features of normal sleep," *Journal of Clinical Neurophysiology: Official Publication of the American Electroencephalographic Society*, vol. 1, no. 3, pp. 253–274, 1984, doi: 10.1097/00004691-198407000-00001.

[2] D. W. Carley and S. S. Farabi, "Physiology of Sleep.," *Diabetes Spectr*, vol. 29, no. 1, pp. 5–9, Feb. 2016, doi: 10.2337/diaspect.29.1.5.

[3] E. Niedermeyer, F. H. Lopes da Silva, S. Vanhatalo, J. Voipio, and K. Kaila, *Electroencephalography: Basic principles, clinical applications, and related fields*, 6th ed. Wolters Kluwer, 2011.

[4] L. Marshall, M. Molle, S. Michaelsen, H. L. Fehm, and J. Born, "Slow potential shifts at sleep--wake transitions and shifts between NREM and REM sleep," *Sleep*, vol. 19, no. 2, pp. 145–151, 1996, doi: 10.1093/sleep/19.2.145.

[5] L. Marshall, M. Mölle, H. L. Fehm, and J. Born, "Scalp recorded direct current brain potentials during human sleep," *The European Journal of Neuroscience*, vol. 10, no. 3, pp. 1167–1178, 1998, doi: 10.1046/j.1460-9568.1998.00131.x.

[6] J. Voipio, P. Tallgren, E. Heinonen, S. Vanhatalo, and K. Kaila, "Millivolt-Scale DC Shifts in the Human Scalp EEG: Evidence for a Nonneuronal Generator," *J Neurophysiol*, vol. 89, no. 4, pp. 2208–2214, 2003, doi: 10.1152/jn.00915.2002.

[7] V. Kiviniemi *et al.*, "Real-time monitoring of human blood-brain barrier disruption," *PloS One*, vol. 12, no. 3, p. e0174072, 2017, doi: 10.1371/journal.pone.0174072.

[8] L. Xie *et al.*, "Sleep drives metabolite clearance from the adult brain," *Science*, vol. 342, no. 6156, pp. 373–377, 2013, doi: 10.1126/science.1241224.

[9] M. Nedergaard, "Garbage Truck of the Brain," *Science*, vol. 340, no. 6140, pp. 1529–1530, 2013, doi: 10.1126/science.1240514.

[10] J. J. Iliff *et al.*, "A Paravascular Pathway Facilitates CSF Flow Through the Brain Parenchyma and the Clearance of Interstitial Solutes, Including Amyloid β," *Sci Transl Med*, vol. 4, no. 147, p. 147ra111, 2012, doi: 10.1126/scitranslmed.3003748.

[11] M. Shibata *et al.*, "Clearance of Alzheimer's amyloid-ss(1-40) peptide from brain by LDL receptor-related protein-1 at the blood-brain barrier.," *J Clin Invest*, vol. 106, no. 12, pp. 1489–99, Dec. 2000, doi: 10.1172/JCI10498.

[12] S. E. Storck *et al.*, "Endothelial LRP1 transports amyloid-β(1-42) across the blood-brain barrier.," *J Clin Invest*, vol. 126, no. 1, pp. 123–36, Jan. 2016, doi: 10.1172/JCI81108.

[13] H. Mestre *et al.*, "Flow of cerebrospinal fluid is driven by arterial pulsations and is reduced in hypertension," *Nature Communications*, vol. 9, p. 4878, 2018, doi: 10.1038/s41467-018-07318-3.

[14] D. A. Nita, S. Vanhatalo, F.-D. Lafortune, J. Voipio, K. Kaila, and F. Amzica, "Nonneuronal origin of CO2-related DC EEG shifts: an in vivo study in the cat," *Journal of Neurophysiology*, vol. 92, no. 2, pp. 1011–1022, 2004, doi: 10.1152/jn.00110.2004.

[15] S. Vanhatalo, J. M. Palva, M. D. Holmes, J. W. Miller, J. Voipio, and K. Kaila, "Infraslow oscillations modulate excitability and interictal epileptic activity in the human cortex during sleep," *Proc Natl Acad Sci U S A*, vol. 101, no. 14, pp. 5053–5057, 2004, doi: 10.1073/pnas.0305375101.

[16] J. Biskamp, M. Bartos, and J.-F. Sauer, "Organization of prefrontal network activity by respiration-related oscillations," *Sci Rep*, vol. 7, no. 1, p. 45508, 2017, doi: 10.1038/srep45508.

[17] B. A. Plog *et al.*, "When the air hits your brain: decreased arterial pulsatility after craniectomy leading to impaired glymphatic flow.," *J Neurosurg*, pp. 1–14, May 2019, doi: 10.3171/2019.2.JNS182675.

[18] D. Purves *et al.*, *Neuroscience, 3rd ed.* Sunderland, MA, US: Sinauer Associates, 2004.

[19] W. J. Schwartz and E. B. Klerman, "Circadian Neurobiology and the Physiologic Regulation of Sleep and Wakefulness," *Neurologic Clinics*, vol. 37, no. 3, pp. 475–486, Aug. 2019, doi: 10.1016/j.ncl.2019.03.001.

[20] E. Aserinsky and N. Kleitman, "Regularly Occurring Periods of Eye Motility, and Concomitant Phenomena, During Sleep," *Science (1979)*, vol. 118, no. 3062, pp. 273–274, Sep. 1953, doi: 10.1126/science.118.3062.273.

[21] D. I. Rubin and J. R. Daube, *Clinical Neurophysiology*. Oxford, UK: Oxford University Press, 2016. doi: 10.1093/med/9780190259631.001.0001.

[22] M. Swartz, "The physiology of the lymphatic system," *Advanced Drug Delivery Reviews*, vol. 50, no. 1–2, pp. 3–20, Aug. 2001, doi: 10.1016/S0169-409X(01)00150-8.

[23] T. Brinker, E. Stopa, J. Morrison, and P. Klinge, "A new look at cerebrospinal fluid circulation.," *Fluids Barriers CNS*, vol. 11, p. 10, 2014, doi: 10.1186/2045-8118-11-10.

[24] R. Daneman and A. Prat, "The blood-brain barrier.," *Cold Spring Harb Perspect Biol*, vol. 7, no. 1, p. a020412, Jan. 2015, doi: 10.1101/cshperspect.a020412.

[25] I. C. M. Verheggen, M. P. J. van Boxtel, F. R. J. Verhey, J. F. A. Jansen, and W. H. Backes, "Interaction between blood-brain barrier and glymphatic system in solute clearance," *Neuroscience & Biobehavioral Reviews*, vol. 90, pp. 26–33, Jul. 2018, doi: 10.1016/j.neubiorev.2018.03.028.

[26] N. A. Aladjalova, "Infra-Slow Rhythmic Oscillations of The Steady Potential of the Cerebral Cortex," *Nature*, vol. 179, no. 4567, pp. 957–959, 1957, doi: 10.1038/179957a0.

[27] N. Birbaumer, T. Elbert, A. G. Canavan, and B. Rockstroh, "Slow potentials of the cerebral cortex and behavior.," *Physiol Rev*, vol. 70, no. 1, pp. 1–41, Jan. 1990, doi: 10.1152/physrev.1990.70.1.1.

[28] H. Caspers, E. J. Speckmann, and A. Lehmenkühler, "DC potentials of the cerebral cortex. Seizure activity and changes in gas pressures.," *Rev Physiol Biochem Pharmacol*, vol. 106, pp. 127–78, 1987.

[29] S. Vanhatalo, J. Voipio, and K. Kaila, "Full-band EEG (FbEEG): an emerging standard in electroencephalography," *Clinical Neurophysiology: Official Journal of the International Federation of Clinical Neurophysiology*, vol. 116, no. 1, pp. 1–8, 2005, doi: 10.1016/j.clinph.2004.09.015.

[30] S. Lecci *et al.*, "Coordinated infraslow neural and cardiac oscillations mark fragility and offline periods in mammalian sleep," *Science Advances*, vol. 3, no. 2, p. e1602026, 2017, doi: 10.1126/sciadv.1602026.

[31] P. Novak, V. Lepicovska, and C. Dostalek, "Periodic amplitude modulation of EEG," *Neuroscience Letters*, vol. 136, no. 2, pp. 213–215, 1992, doi: 10.1016/0304-3940(92)90051-8.

[32] Y. Nir *et al.*, "Interhemispheric correlations of slow spontaneous neuronal fluctuations revealed in human sensory cortex," *Nature Neuroscience*, vol. 11, no. 9, pp. 1100–1108, 2008, doi: 10.1038/nn.2177.

[33] F. Amzica and M. Steriade, "Neuronal and Glial Membrane Potentials during Sleep and Paroxysmal Oscillations in the Neocortex," *Journal of Neuroscience*, vol. 20, no. 17, pp. 6648–6665, 2000.

[34] G. G. Somjen, "Electrogenesis of sustained potentials," *Progress in Neurobiology*, vol. 1, pp. 199–237, Jan. 1973, doi: 10.1016/0301-0082(73)90012-9.

[35] R. D. Tschirgi and J. L. Taylor, "Slowly Changing Bioelectric Potentials Associated With the Blood-Brain Barrier," *American Journal of Physiology-Legacy Content*, vol. 195, no. 1, pp. 7–22, Sep. 1958, doi: 10.1152/ajplegacy.1958.195.1.7.

[36] T. F. Hornbein and S. C. Sorensen, "d-c Potential difference between different cerebrospinal fluid sites and blood in dogs.," *Am J Physiol*, vol. 223, no. 2, pp. 415–8, Aug. 1972, doi: 10.1152/ajplegacy.1972.223.2.415.

[37] P. A. Revest, H. C. Jones, and N. J. Abbott, "The transendothelial DC potential of rat blood-brain barrier vessels in situ," *Advances in Experimental Medicine and Biology*, vol. 331, pp. 71–74, 1993, doi: 10.1007/978-1-4615-2920-0_12.

[38] S. Vanhatalo *et al.*, "Scalp-recorded slow EEG responses generated in response to hemodynamic changes in the human brain," *Clinical Neurophysiology*, vol. 114, no. 9, pp. 1744–1754, 2003, doi: 10.1016/s1388-2457(03)00163-9.

[39] J. M. Besson, C. D. Woody, P. Aleonard, H. K. Thompson, D. Albe-Fessard, and W. H. Marshall, "Correlations of brain d-c shifts with changes in cerebral blood flow," *The American Journal of Physiology*, vol. 218, no. 1, pp. 284–291, 1970, doi: 10.1152/ajplegacy.1970.218.1.284.

[40] A. Hyvärinen, J. Karhunen, and E. Oja, *Independent Component Analysis*. John Wiley Sons Inc, 2001.

[41] J. M. Palva and S. Palva, "Functional integration across oscillation frequencies by cross-frequency phase synchronization," *European Journal of Neuroscience*, vol. 48, no. 7, pp. 2399–2406, Oct. 2018, doi: 10.1111/ejn.13767.

[42] V. v Nikulin and T. Brismar, "Phase synchronization between alpha and beta oscillations in the human electroencephalogram.," *Neuroscience*, vol. 137, no. 2, pp. 647–57, 2006, doi: 10.1016/j.neuroscience.2005.10.031.

[43] J. M. Palva, S. Palva, and K. Kaila, "Phase synchrony among neuronal oscillations in the human cortex," *J Neurosci*, vol. 25, no. 15, pp. 3962–3972, 2005, doi: 25/15/3962 [pii].

[44] R. T. Canolty and R. T. Knight, "The functional role of cross-frequency coupling," *Trends in Cognitive Sciences*, vol. 14, no. 11, pp. 506–515, Nov. 2010, doi: 10.1016/j.tics.2010.09.001.

[45] W. Singer, "Neuronal Synchrony: A Versatile Code for the Definition of Relations?," *Neuron*, vol. 24, no. 1, pp. 49–65, Sep. 1999, doi: 10.1016/S0896-6273(00)80821-1.

[46] M. Lobier, F. Siebenhühner, S. Palva, and J. M. Palva, *Phase Transfer Entropy: A novel phase-based measure for directed connectivity in networks coupled by oscillatory interactions*, vol. 85. 2013. doi: 10.1016/j.neuroimage.2013.08.056.

[47] N. M. Timme and C. Lapish, "A Tutorial for Information Theory in Neuroscience," *eNeuro*, vol. 5, no. 3, 2018, doi: 10.1523/ENEURO.0052-18.2018.

[48] T. Bossomaier, L. Barnett, M. Harré, and J. T. Lizier, *An Introduction to Transfer Entropy: Information Flow in Complex Systems*. Springer International Publishing, 2016. [Online]. Available: https://www.springer.com/gp/book/9783319432212

[49] V. Korhonen *et al.*, "Synchronous Multiscale Neuroimaging Environment for Critically Sampled Physiological Analysis of Brain Function: Hepta-Scan Concept," *Brain Connectivity*, vol. 4, no. 9, pp. 677–689, 2014, doi: 10.1089/brain.2014.0258.

[50] S. G. Horovitz *et al.*, "Decoupling of the brain's default mode network during deep sleep," *Proceedings of the National Academy of Sciences - PNAS*, vol. 106, no. 27, pp. 11376–11381, 2009, [Online]. Available: https://agris.fao.org/agris-search/search.do?recordID=US201301653150

[51] C. Kaufmann *et al.*, "Brain activation and hypothalamic functional connectivity during human non-rapid eye movement sleep: an EEG/fMRI study," *Brain: A Journal of Neurology*, vol. 129, no. Pt 3, pp. 655–667, 2006, doi: 10.1093/brain/awh686.

[52] P. J. Allen, O. Josephs, and R. Turner, "A method for removing imaging artifact from continuous EEG recorded during functional MRI," *Neuroimage*, vol. 12, no. 2, pp. 230–239, 2000, doi: 10.1006/nimg.2000.0599 [doi].

[53] E. Huigen, A. Peper, and C. Grimbergen, "Investigation into the origin of the noise of surface electrodes," *Med Biol Eng Comput*, vol. 40, pp. 332–338, 2002, doi: 10.1007/BF02344216.

[54] A. Hyvärinen, "Fast and robust fixed-point algorithms for independent component analysis," *IEEE Transactions on Neural Networks*, vol. 10 3, pp. 626–634, 1999.

[55] A. de Cheveigné and D. Arzounian, "NeuroImage," *Neuroimage*, vol. 172, pp. 903–912, 1992, [Online]. Available: https://www.sciencedirect.com/science/article/pii/S1053811918300351

[56] M. X. Cohen, *Analyzing Neural Time Series Data*. The MIT Press, 2014. doi: 10.7551/mitpress/9609.001.0001.

[57] S. Monto, S. Palva, J. Voipio, and J. M. Palva, "Very Slow EEG Fluctuations Predict the Dynamics of Stimulus Detection and Oscillation Amplitudes in Humans," *Journal of Neuroscience*, vol. 28, no. 33, pp. 8268–8272, 2008.

[58] J.-P. Lachaux, E. Rodriguez, J. Martinerie, and F. J. Varela, "Measuring phase synchrony in brain signals," *Human Brain Mapping*, vol. 8, no. 4, pp. 194–208, 1999, doi: https://doi.org/10.1002/(SICI)1097-0193(1999)8:4<194::AID-HBM4>3.0.CO;2-C.

[59] D. W. Scott, "On optimal and data-based histograms," *Biometrika*, vol. 66, no. 3, pp. 605–610, 1979, doi: 10.1093/biomet/66.3.605.

[60] Y. Benjamini and Y. Hochberg, "Controlling the False Discovery Rate: A Practical and Powerful Approach to Multiple Testing," *Journal of the Royal Statistical Society. Series B (Methodological)*, vol. 57, no. 1, pp. 289–300, 1995, [Online]. Available: https://www.jstor.org/stable/2346101

[61] J. Theiler, S. Eubank, A. Longtin, B. Galdrikian, and J. Doyne Farmer, "Testing for nonlinearity in time series: the method of surrogate data," *Physica D: Nonlinear Phenomena*, vol. 58, no. 1, pp. 77–94, 1992, doi: 10.1016/0167-2789(92)90102-S.

[62] C. O. Fritz, P. E. Morris, and J. J. Richler, "Effect size estimates: Current use, calculations, and interpretation.," *Journal of Experimental Psychology: General*, vol. 141, no. 1, pp. 2–18, 2012, doi: 10.1037/a0024338.

[63] R. v Ceguerra, J. T. Lizier, and A. Y. Zomaya, "Information storage and transfer in the synchronization process in locally-connected networks," in *2011 IEEE Symposium on Artificial Life (ALIFE)*, pp. 54–61. doi: 10.1109/ALIFE.2011.5954653.

[64] N. Ay and D. Polani, "Information flows in causal networks," *Advances in Complex Systems, v.11, 17-41 (2008)*, vol. 11, Feb. 2008.

[65] M. Massimini, F. Ferrarelli, R. Huber, S. K. Esser, H. Singh, and G. Tononi, "Breakdown of cortical effective connectivity during sleep," *Science*, vol. 309, no. 5744, pp. 2228–2232, 2005, doi: 10.1126/science.1117256.

[66] R. Vicente, M. Wibral, M. Lindner, and G. Pipa, "Transfer entropy—a model-free measure of effective connectivity for the neurosciences," *J Comput Neurosci*, vol. 30, no. 1, pp. 45–67, Feb. 2011, doi: 10.1007/s10827-010-0262-3.

[67] D. Cumin and C. P. Unsworth, "Generalising the Kuramoto model for the study of neuronal synchronisation in the brain," *Physica D: Nonlinear Phenomena*, vol. 226, no. 2, pp. 181–196, Feb. 2007, doi: 10.1016/j.physd.2006.12.004.

[68] S. Dreha-Kulaczewski, A. A. Joseph, K.-D. Merboldt, H.-C. Ludwig, J. Gärtner, and J. Frahm, "Inspiration Is the Major Regulator of Human CSF Flow," *Journal of Neuroscience*, vol. 35, no. 6, pp. 2485–2491, 2015.

[69] S. Dreha-Kulaczewski, A. A. Joseph, K.-D. Merboldt, H.-C. Ludwig, J. Gärtner, and J. Frahm, "Identification of the Upward Movement of Human CSF In Vivo and its Relation to the Brain Venous System," *Journal of Neuroscience*, vol. 37, no. 9, pp. 2395–2402, 2017.

[70] J. Kananen *et al.*, "Respiratory-related brain pulsations are increased in epilepsy—a two-centre functional MRI study," *Brain Communications*, vol. 2, no. 2, p. fcaa076, 2020, doi: 10.1093/braincomms/fcaa076.

[71] C. Zelano *et al.*, "Nasal Respiration Entrains Human Limbic Oscillations and Modulates Cognitive Function," *Journal of Neuroscience*, vol. 36, no. 49, pp. 12448–12467, 2016.

[72] J. L. Herrero, S. Khuvis, E. Yeagle, M. Cerf, and A. D. Mehta, "Breathing above the brain stem: volitional control and attentional modulation in humans," *Journal of Neurophysiology*, vol. 119, no. 1, pp. 145–159, 2018, doi: 10.1152/jn.00551.2017.

[73] F. Ding, J. O'Donnell, Q. Xu, N. Kang, N. Goldman, and M. Nedergaard, "Changes in the composition of brain interstitial ions control the sleep-wake cycle," *Science*, vol. 352, no. 6285, pp. 550–555, 2016, doi: 10.1126/science.aad4821.

[74] L. Raitamaa *et al.*, "Spectral analysis of physiological brain pulsations affecting the BOLD signal.," *Hum Brain Mapp*, vol. 42, no. 13, pp. 4298–4313, Sep. 2021, doi: 10.1002/hbm.25547.

[75] J. Yang *et al.*, "Loss of astrocyte polarization in the tg-ArcSwe mouse model of Alzheimer's disease," *Journal of Alzheimer's disease: JAD*, vol. 27, no. 4, pp. 711–722, 2011, doi: 10.3233/JAD-2011-110725.

[76] M. Arbel-Ornath *et al.*, "Interstitial fluid drainage is impaired in ischemic stroke and Alzheimer's disease mouse models," *Acta Neuropathologica*, vol. 126, no. 3, pp. 353–364, 2013, doi: 10.1007/s00401-013-1145-2.

[77] R. O. Carare *et al.*, "Immune complex formation impairs the elimination of solutes from the brain: implications for immunotherapy in Alzheimer's disease," *Acta Neuropathologica Communications*, vol. 1, p. 48, 2013, doi: 10.1186/2051-5960-1-48.

[78] T. Eid *et al.*, "Loss of perivascular aquaporin 4 may underlie deficient water and K+ homeostasis in the human epileptogenic hippocampus," *Proc Natl Acad Sci U S A*, vol. 102, no. 4, pp. 1193–1198, 2005, doi: 10.1073/pnas.0409308102.

[79] E. A. van Vliet, E. Aronica, and J. A. Gorter, "Blood-brain barrier dysfunction, seizures and epilepsy," *Seminars in Cell & Developmental Biology*, vol. 38, pp. 26–34, 2015, doi: 10.1016/j.semcdb.2014.10.003.

[80] N. Marchi, M. Banjara, and D. Janigro, "Blood-brain barrier, bulk flow, and interstitial clearance in epilepsy," *Journal of Neuroscience Methods*, vol. 260, pp. 118–124, 2016, doi: 10.1016/j.jneumeth.2015.06.011.

[81] W. Pan and A. J. Kastin, “The Blood-Brain Barrier: Regulatory Roles in Wakefulness and Sleep.,” *Neuroscientist*, vol. 23, no. 2, pp. 124–136, 2017, doi: 10.1177/1073858416639005.

[82] J. J. Iliff *et al.*, “Impairment of Glymphatic Pathway Function Promotes Tau Pathology after Traumatic Brain Injury,” *The Journal of Neuroscience*, vol. 34, no. 49, pp. 16180–16193, Dec. 2014, doi: 10.1523/JNEUROSCI.3020-14.2014.

[83] P. K. Eide, V. Vinje, A. H. Pripp, K.-A. Mardal, and G. Ringstad, “Sleep deprivation impairs molecular clearance from the human brain.,” *Brain*, vol. 144, no. 3, pp. 863–874, 2021, doi: 10.1093/brain/awaa443.